NAVAL POSTGRADUATE SCHOOL

MONTEREY, CALIFORNIA

THESIS

CALIBRATION AND VALIDATION OF INERTIAL MEASUREMENT UNIT FOR WAVE RESOLVING DRIFTERS

by

Jeffrey R. Portell

December 2013

Thesis Advisor: Thomas H. C. Herbers
Second Reader: James Calusdian

Approved for public release; distribution is unlimited

THIS PAGE INTENTIONALLY LEFT BLANK

REPORT DOCUMENTATION PAGE			Form Approved OMB No. 0704-0188

1. AGENCY USE ONLY *(Leave blank)*	2. REPORT DATE December 2013	3. REPORT TYPE AND DATES COVERED Master's Thesis

4. TITLE AND SUBTITLE CALIBRATION AND VALIDATION OF INERTIAL MEASUREMENT UNIT FOR WAVE RESOLVING DRIFTERS	5. FUNDING NUMBERS
6. AUTHOR(S) Jeffrey R. Portell	
7. PERFORMING ORGANIZATION NAME(S) AND ADDRESS(ES) Naval Postgraduate School Monterey, CA 93943-5000	8. PERFORMING ORGANIZATION REPORT NUMBER
9. SPONSORING /MONITORING AGENCY NAME(S) AND ADDRESS(ES) N/A	10. SPONSORING/MONITORING AGENCY REPORT NUMBER

11. SUPPLEMENTARY NOTES The views expressed in this thesis are those of the author and do not reflect the official policy or position of the Department of Defense or the U.S. Government. IRB protocol number ____N/A____.

12a. DISTRIBUTION / AVAILABILITY STATEMENT Approved for public release; distribution is unlimited	12b. DISTRIBUTION CODE A

13. ABSTRACT (maximum 200 words)

We examine the performance of the Yost Engineering Incorporated 3-Space Sensor Data-Logging (TSS-DL) for use in wave resolving drifters (WRDs) that collect ocean surface wave data. We create a surface wave orbital motion simulator to test the TSS-DL in a controlled, laboratory setting at the Naval Postgraduate School. Tests are conducted in three different configurations at five frequencies within the swell and wind-sea bands. Results from the tests show that the TSS-DL can accurately resolve the vertical simulated wave motions to within $\pm$ 3–7% of the analytic signal amplitude and can resolve the horizontal simulated wave motions to within $\pm$ 21–33% of the analytic signal amplitude. We further examine some field data collected using the TSS-DL onboard WRDs deployed in June 2013 near the mouth of the Columbia River. This analysis, based on comparison with independent GPS wave measurements, demonstrates that the TSS-DL yields reliable estimates of surface wave spectra and can track surface wave profiles even under extreme conditions with large breaking waves. Overall, this study shows that the TSS-DL is a suitable sensor for use in ocean surface drifters to accurately record surface waves.

14. SUBJECT TERMS Ocean waves, wave buoys, drifters, inertial measurement units, MEMS, sensor validation, reference frames, quaternions, wave orbital motion, mouth of the Columbia River	15. NUMBER OF PAGES 81
	16. PRICE CODE

17. SECURITY CLASSIFICATION OF REPORT	18. SECURITY CLASSIFICATION OF THIS PAGE	19. SECURITY CLASSIFICATION OF ABSTRACT	20. LIMITATION OF ABSTRACT
Unclassified	Unclassified	Unclassified	UU

NSN 7540-01-280-5500 Standard Form 298 (Rev. 2-89)
Prescribed by ANSI Std. 239-18

THIS PAGE INTENTIONALLY LEFT BLANK

Approved for public release; distribution is unlimited

CALIBRATION AND VALIDATION OF INERTIAL MEASUREMENT UNIT FOR WAVE RESOLVING DRIFTERS

Jeffrey R. Portell
Lieutenant, United States Navy
B.S., United States Naval Academy, 2004

Submitted in partial fulfillment of the
requirements for the degree of

MASTER OF SCIENCE IN METEOROLOGY AND OCEANOGRAPHY

from the

NAVAL POSTGRADUATE SCHOOL
December 2013

Author: Jeffrey R. Portell

Approved by: Thomas H. C. Herbers
Thesis Advisor

James Calusdian
Second Reader

Peter C. Chu
Chair, Department of Oceanography

THIS PAGE INTENTIONALLY LEFT BLANK

ABSTRACT

We examine the performance of the Yost Engineering Incorporated 3-Space Sensor Data-Logging (TSS-DL) for use in wave resolving drifters (WRDs) that collect ocean surface wave data. We create a surface wave orbital motion simulator to test the TSS-DL in a controlled, laboratory setting at the Naval Postgraduate School. Tests are conducted in three different configurations at five frequencies within the swell and wind-sea bands. Results from the tests show that the TSS-DL can accurately resolve the vertical simulated wave motions to within $\pm$ 3–7% of the analytic signal amplitude and can resolve the horizontal simulated wave motions to within $\pm$ 21–33% of the analytic signal amplitude. We further examine some field data collected using the TSS-DL onboard WRDs deployed in June 2013 near the mouth of the Columbia River. This analysis, based on comparison with independent GPS wave measurements, demonstrates that the TSS-DL yields reliable estimates of surface wave spectra and can track surface wave profiles even under extreme conditions with large breaking waves. Overall, this study shows that the TSS-DL is a suitable sensor for use in ocean surface drifters to accurately record surface waves.

THIS PAGE INTENTIONALLY LEFT BLANK

TABLE OF CONTENTS

THIS PAGE INTENTIONALLY LEFT BLANK

LIST OF FIGURES

LIST OF TABLES

THIS PAGE INTENTIONALLY LEFT BLANK

LIST OF ACRONYMS AND ABBREVIATIONS

AHRS	attitude and heading reference system
COTS	commercial off-the-shelf
CPSD	cross power spectral density
DWR-G	Datawell Directional Waverider GPS-based buoy
GPS	global positioning system
GUI	graphical user interface
IMU	inertial measurement unit
MCR	mouth of the Columbia River
MEMS	microelectromechanical systems
METOC	meteorology and oceanography
NPS	Naval Postgraduate School
PSD	power spectral density
RF	radio frequency
R/V	research vessel
SNR	signal to noise ratio
SWOMS	surface wave orbital motion simulator
TSS-DL	3-space sensor data-logging
WRD	wave resolving drifter
WRD-A	wave resolving drifter—alpha variant
WRD-B	wave resolving drifter—bravo variant
YEI	Yost Engineering Incorporated

THIS PAGE INTENTIONALLY LEFT BLANK

ACKNOWLEDGMENTS

I would first like to thank my advisor, Professor Tom Herbers, for his guidance, instruction, and patience throughout this process. It has been an honor to work with such a talented mind in the classroom, in the lab, and in the field. His knowledge seems to be without limit and I have learned a great deal from him. Thank you Sir!

I would also like to thank my second reader, James Calusdian, for his guidance, assistance, and patience in introducing me to the world of quaternions and reference frame transformations, no easy task to be sure. He was also instrumental in the assembly of the technical components of the SWOMS, and for that I am very grateful. Thank you Sir!

I would like to thank my colleague, and more importantly my friend, LCDR Doug Pearman. He has been exceptionally helpful in providing inspiration, guidance, assistance, and motivation throughout, and I am truly thankful to have had the opportunity to work with him and his brilliant mind in the academic realm. I wish him good fortune in his PhD work and look forward to working with him again in the fleet. Thank you Sir!

I would like to thank Paul Jessen for all of his assistance and support with the construction of the SWOMS and in helping me through the nightmare known as MATLAB. It was an honor to work with him in the field as well. Thank you Sir!

To all of my professors here at NPS who have taught me, challenged me, and made me better, thank you!

Finally I would like to thank my family for their support in all of my endeavors. Most especially I want to thank my wife, Lydia, for her love, support, and patience from beginning to end. Thanks darling, I love you!

THIS PAGE INTENTIONALLY LEFT BLANK

I. INTRODUCTION

Understanding ocean surface waves is fundamental to our ability to develop predictive models of sea state, nearshore processes, and other oceanographic and atmospheric phenomena. Ocean surface waves are one of the most tangible oceanographic features and have significant societal impacts, from the safety and navigation of all manner of ocean vessels (e.g., tankers, container ships, Naval warships, recreational watercraft, etc.) to the transformation of the shoreline (e.g., beach erosion, sediment relocation, impacts to jetties, etc.). Additionally, the interaction of ocean surface waves with other oceanographic features is an area of ongoing study. How ocean surface waves interact with currents is a topic actively being investigated to better understand the occurrence of extreme wave events as incoming ocean swell encounter the flow of ebb currents in coastal inlets and river mouths. Extreme "rogue" waves are known to occur, yet the physics and dynamics of how a nonlinear wave field evolves in space and time remains poorly understood (Janssen and Herbers 2009). In order to further the understanding of these phenomena and develop predictive models, accurate in-situ field measurements are needed. Collection of ocean surface wave data is also important for real time monitoring of environmental conditions near beaches, harbors, and inlets.

The motivation for this thesis is to enhance the ability to collect accurate, reliable, low cost in-situ measurements of ocean surface waves. The specific objective is to examine the use of the Yost Engineering Incorporated (YEI) 3-Space Sensor Data-Logging (TSS-DL) in wave resolving drifters (WRDs) for the collection of surface wave orbital motion data. To accomplish this, the TSS-DL is tested in a controlled, laboratory setting to diagnose the accuracy of its measurements of simulated surface wave orbital motions. In conjunction with the laboratory testing, algorithms were applied to the data collected by the TSS-DL to determine whether we are able to improve the quality and usefulness of the data. Finally we analyze field data collected by the TSS-DL to assess

its accuracy. In this chapter we first give some background on the importance and challenges of collecting wave data, followed by a review of previous studies utilizing buoys or drifters for wave measurements.

A. WAVE DATA COLLECTION IN COASTAL INLETS AND RIVER MOUTHS

The most common method for ocean surface wave data collection is the use of buoys, either moored or drifting. Moored buoys collect surface wave data at a single spatial point (i.e., an Eulerian approach) and are typically larger than drifters to accommodate batteries for longer data collection times. Drifting buoys drift along the surface with the prevailing surface current (i.e., a Lagrangian approach), can be deployed upstream of a desired data collection location, and must be tracked in order to know the drifters present location for recovery.

There are numerous challenges related to surface wave data collection in tidal inlets and river mouths via moored buoys. These challenges revolve around the deployment, presence, and subsequent recovery of the buoys. Pearman et al. (2013) highlight some of these challenges such as current drag on mooring lines and interference from ship traffic. Furthermore, the occurrence of extreme wave events as ocean swell opposes ebb flows from river mouths can complicate matters. These factors and others hinder our ability to safely maneuver a vessel on-station, safely deploy and recover moored buoys, and obtain accurate and reliable surface wave data from the buoys.

Another challenge for surface wave data collection involves the high costs associated with moored buoys. The cost depends on factors such as the number, size, and sophistication of the buoy(s) being used. For large, specialized buoys the overall cost can increase due to the higher cost of the buoy itself, the need for a large vessel equipped with a crane or A-frame capable of mooring and recovering the buoy, the need for a forklift for transporting the buoy pier-side, and all of the other supplementary costs that go with these such as the crew, fuel, food, and so on. This makes the procurement and/or

utilization of some moored buoys cost prohibitive. Therefore, the ability to reduce the instrument unit cost and facilitate deployment/recovery from a small vessel is of high importance.

B. NAVAL RELEVANCE

Safety and cost effectiveness are concerns for the U.S. Navy, as well. Investing significant capital and man-hours into planning and attempting to execute exercises and operations can be all for naught when environmental conditions prohibit their execution. Moreover, the safety of all evolutions, from simply transiting from one point to another to conducting complex, multi-national exercises, is paramount. The ability for naval meteorology and oceanography (METOC) to characterize environmental conditions such as sea state and significant wave height both spatially and temporally has direct impacts on these two elements. The collection and analysis of surface wave data is crucial for both environmental model input as well as validation of model output, which in turn affects METOC's ability to accurately and reliably characterize the environment. Having low cost, easily deployable buoys for surface wave data collection, particularly in areas where data have not been collected, is difficult to collect, and in which the Navy frequently operates (e.g., tidal inlets and river mouths), is an integral part of our overall data collection strategy.

C. BUOYS AND DRIFTERS

1. Datawell Waverider Buoy

One of the standard tools for measuring ocean surface waves is the Datawell Waverider buoy. Throughout the rest of this thesis, we will specifically refer to the Datawell Directional Waverider Global Positioning System (GPS) based Buoy, or DWR-G (see Figure 1). The DWR-G uses the Doppler frequency shift of the GPS signal to calculate velocities, which are then integrated over time via patented algorithms to calculate the motions, and hence displacements, of the buoy. The DWR-G samples at a rate of 2Hz, which is converted to 1.28Hz for horizontal and vertical motions to correspond to its transmitter data format, is accurate to within 0.01m for both horizontal and vertical displacements, and is able to measure waves in the frequency range of

0.01Hz (100s period) to 0.64Hz (1.6s period) (Datawell 2010). Datawell Waverider buoys are rugged, accurate, and specifically tailored for the collection of surface wave data. The cost for one of these buoys depending on the size and options can range from $15K–40K, and the weight can range from 37.4–209lbs (0.4m and 0.7m diameter DWR-G, respectively). While the DWR-G is capable of being moored, our use of the DWR-G for the remainder of this thesis is in a surface drifting mode. Given the cost for an individual DWR-G, along with its size and weight, the DWR-G is not ideally suited for the coastal inlet/river mouth environment where it can be cumbersome to deploy and recover from small vessels, is subjected to potential damage from heavy ship traffic, and runs the risk of being damaged or stolen if beached along the nearby shoreline.

Figure 1. Datawell Directional Waverider GPS-based (DWR-G) 0.4m buoy (from Datawell 2013).

2. Surface Drifters and GPS

The concept of observing objects floating on the ocean surface to glean information about oceanographic phenomena dates back to Stommel in the late 1940s and even back to Benjamin Franklin in the late 1700s (Davis 1991). In more recent history

the use of surface drifting objects to collect oceanographic data has become more sophisticated as researchers seek new ways to keep costs down while incorporating the latest in technological advances. The use of commercial off-the-shelf (COTS) materials, hardware, and sensors has led to the development of inexpensive drifters suitable for deployment in large numbers. In 2002 and 2003, the use of polyvinyl chloride pipe as a durable shell and a GPS sensor for position and velocity data of a surface drifter was successfully tested in the nearshore and surf zones (see Figure 2) (Schmidt et al. 2002; Johnson et al. 2003). MacMahan et al. (2009) further reduced costs using hand-held GPS receivers with internal power and data logging capability. While these drifters successfully tracked surface currents, the GPS receivers available at that time could not resolve the wave orbital motion.

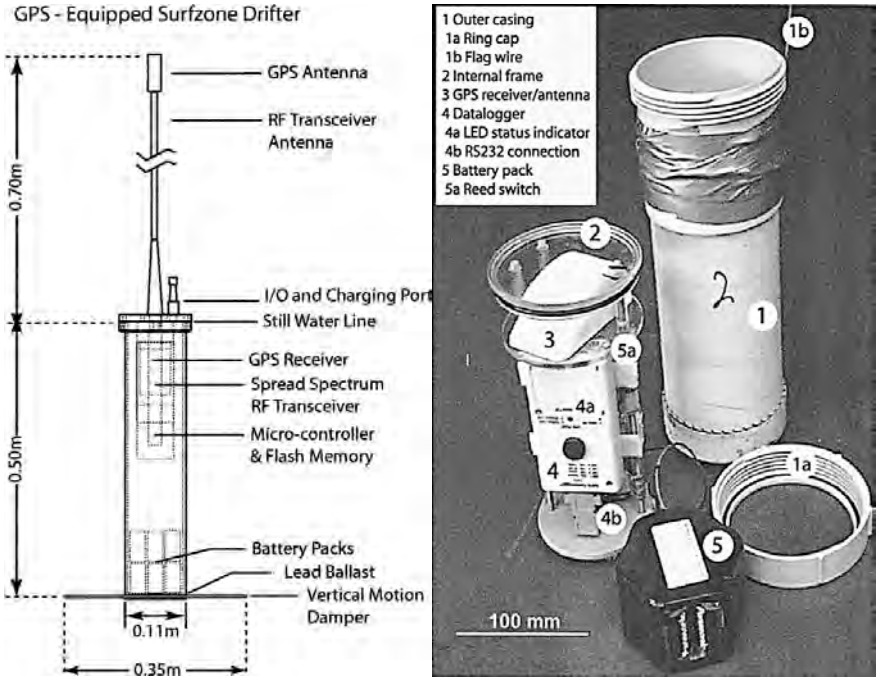

Figure 2. At left: schematic of surf zone drifter (from Schmidt et al. 2003). At right: Photograph of COTS GPS drifter (from Johnson et al. 2003).

At the Naval Postgraduate School (NPS) in 2010, Herbers et al. (2012) developed a prototype wave resolving drifter (WRD) comprised of a COTS GPS receiver, a battery pack, and a radio frequency (RF) transmitter packaged in a small Pelican case and sitting

atop an in-house fabricated drifting buoy made of polyethylene closed cell foam discs and Delrin plates (see Figure 3). With this inexpensive, easily handled and deployable drifter, they were able to resolve vertical and horizontal wave orbital displacements from which spectral estimates of wave energy, mean direction, and directional spread could be extracted, all of which showed good agreement with the standard Datawell buoys.

Figure 3. Prototype wave resolving drifter (WRD) (from Herbers et al. 2012).

II. WAVE RESOLVING DRIFTERS AND THE 3-SPACE SENSOR DATA-LOGGING

In order to reduce the bulky footprint of a GPS unit and its external antenna such as the one shown in Figure 3, accelerometers were investigated to resolve vertical motions. Here we review some versions of the WRDs developed at NPS and their associated sensors.

A. WRD—ALPHA

The first generation WRD developed at NPS, the "alpha" variant or WRD-A (see Figure 4), was created in 2012 and consists of a spherical, hard shell closed-cell foam core buoy 0.3m in diameter, with ballast weight suspended beneath the buoy and a collection of sensors externally affixed to the buoy. The attached sensors include a Locosys GT-31 GPS receiver, a Gulf Coast Data Concepts X6-2 three-axis accelerometer mounted vertically between the buoy and the ballast weight, and a Garmin DC 40 GPS-enabled transmitter (Pearman et al. 2013). The primary objective of the WRD-A is to resolve as accurately as possible surface wave orbital motions while freely drifting through tidal inlets and river mouths. To facilitate deployment in large numbers it is important to keep costs down through the utilization of COTS components and by creating lighter weight, easily deployable/recoverable drifters.

Figure 4. WRD-A (from McIntyre 2013).

The function of the GT-31 (see Figure 5) is two-fold; first, as its clock is the most precise among the sensors, it serves as the source for the time that all data will ultimately be analyzed in; second, it serves to resolve the horizontal surface drift and wave orbital displacements via differential position data and Doppler velocity data. Comparisons with horizontal surface wave orbital displacements measured with a DWR-G buoy show excellent agreement across the swell frequency range (Pearman et al. 2013).

Figure 5. Locosys GT-31 GPS receiver.

The function of the X6-2 (see Figure 6) is to better resolve vertical surface wave orbital displacements than those obtained with the GT-31. The X6-2 is an accelerometer, not an inertial measurement unit (IMU). As such, it is incapable of resolving its own orientation and thus unable to remove or mitigate errors in the vertical accelerations caused by projected accelerations from other axes induced by pitch and/or roll of the sensor. Results from comparisons between the vertical surface wave orbital displacements from the DWR-G data and the WRD-A data show good agreement, although the X6-2 has a tendency to overestimate the swell peaks and troughs. Without another sensor such as a magnetometer or gyroscope it is not possible to resolve this difference in amplitude (Pearman et al. 2013).

Figure 6. Gulf Coast Data Concepts X6-2 accelerometer.

The function of the DC 40 (see Figure 7) is merely to facilitate real-time tracking of the WRD-A, which has proven necessary particularly during the recovery of the drifter. To further aid in recovery a NaviSafe marine light (see Figure 7) is also affixed to the drifter.

Figure 7. (left) Garmin DC 40 GPS-enabled transmitter. (right) NaviSafe marine light.

The cost to produce a fully-equipped WRD-A is less than $1K, making it approximately 15–40 times less expensive than the DWR-G and thus very attractive for deployments in large numbers or low cost routine wave monitoring applications. While the quality of the data collected by a WRD-A is slightly less than that from a DWR-G, it shows good agreement overall while leaving some room for improvement.

B. WRD—BRAVO

Using the WRD-A and its primary objective as a baseline, NPS set out to improve both the design and sensor package onboard the second iteration of the WRD; the "bravo" variant or WRD-B (see Figure 8). Like its predecessor, the WRD-B maintains a lightweight, easily deployable/recoverable footprint while still keeping the cost under $1K. All of the materials used in the creation of the WRD-B (i.e., acrylic, Delrin, 316 stainless steel hardware, rubber, silicone gel, adhesive sealant, foam insulation, and Velcro) are non-magnetic, which will be noteworthy later as we discuss the sensors. The WRD-B is a hollow spherical buoy 0.254m (10") in diameter created by two 0.006m (1/4") thick acrylic hemispheres secured together. The edge of each hemisphere flares out 90 degrees into a 0.025m (1") ring, which creates a total diameter of 0.305m (12") including the ring. The hemispheres are locked together at these rings, which are secured with six bolts. Between the rings of the hemispheres is placed a 0.003m (1/8") thick rubber gasket that is lightly coated with a silicone gel to ensure watertight integrity at the closure point.

Figure 8. WRD-B.

Through the bottom of the buoy is threaded a 0.019m (3/4”) diameter eyebolt, to which ballast weight in the form of chain-links are attached via locking carabiners. Inside the bottom hemisphere are mounted two Delrin plates, one 0.178m (7”) in diameter and one 0.241m (9.5”) in diameter. The smaller plate, which is mounted lower in the hemisphere, is primarily secured with the terminating end of the ballast weight eyebolt and adhesive sealant around the edge. Below the smaller plate the hemisphere is filled with foam insulation that serves to additionally secure the plate and to provide additional watertight integrity at the point where the ballast weight eyebolt penetrates the lower hemisphere. The ballast weight eyebolts’ primary means of watertight integrity comes from the rubber washers used in securing it. The larger plate is mounted above the smaller plate and is secured in place by four bolts that connect it to the lower plate. This larger plate serves as the platform on which the WRD-B’s sensors are mounted (see Figure 9).

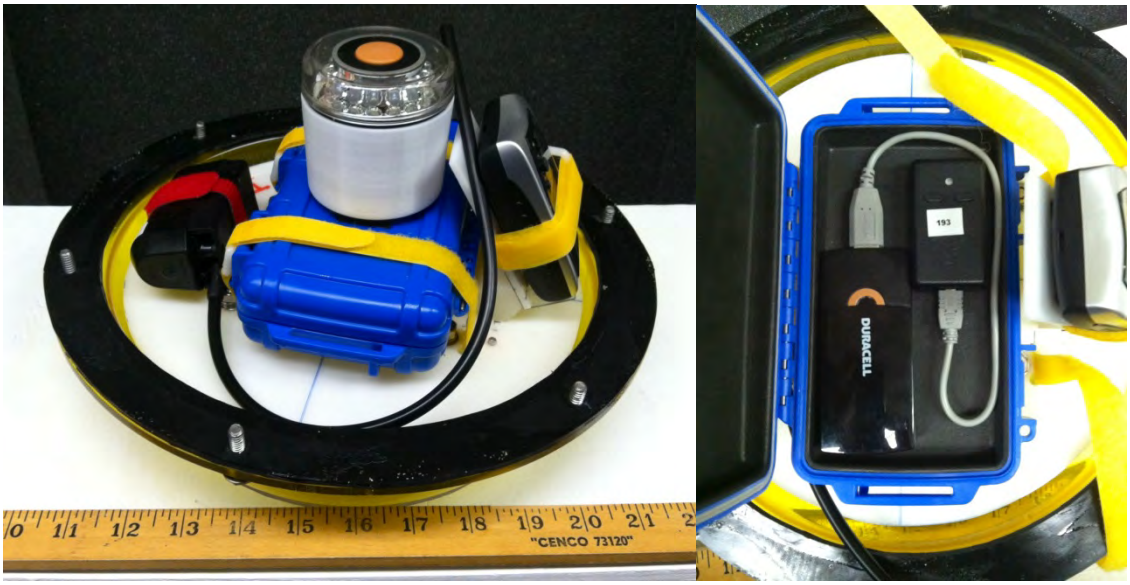

Figure 9. (left) WRD-B sensor package. (right) TSS-DL and battery pack mounted in Otterbox in WRD-B.

The sensor package housed inside the WRD-B contains some common sensors to the WRD-A. The GT-31 GPS receiver is utilized once again to record accurate time and to provide quality data on the horizontal surface wave orbital displacements. The Garmin DC 40 GPS-enabled transmitter is also incorporated for real-time tracking of the WRD-B, along with a NaviSafe marine light. The most significant change to the sensor package is the replacement of the X6-2 accelerometer with the YEI TSS-DL (see Figure 10).

Figure 10. YEI TSS-DL.

C. TSS-DL

The YEI TSS-DL (see Figure 11) is a miniature attitude and heading reference system (AHRS). As an AHRS, it is able to resolve its absolute orientation or its orientation relative to a reference frame. To accomplish this, the TSS-DL has at its core a highly precise and reliable IMU. The IMU, along with onboard sophisticated, proprietary algorithms transforms the TSS-DL from simply an IMU to an AHRS. Outputs from both the IMU and AHRS aspects of the TSS-DL will be analyzed in this thesis.

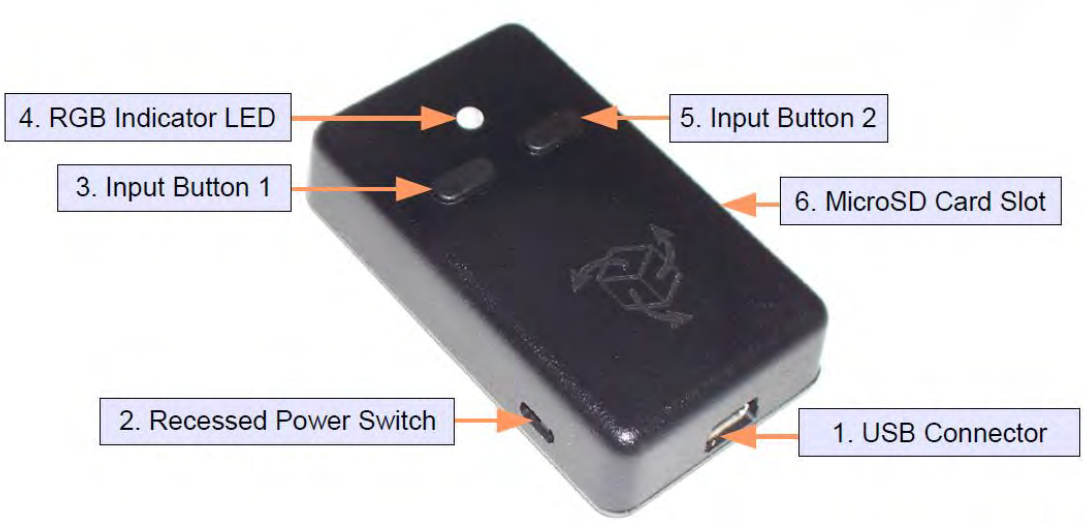

Figure 11. TSS-DL features (from YEI Technologies 2013a).

The IMU is composed of multiple microelectromechanical systems (MEMS), including a triaxial accelerometer, a triaxial gyroscope, and a triaxial magnetometer. The triaxial accelerometer measures accelerations along all three axes in units of g-force, the triaxial gyroscope measures angular motion about all three axes in units of radians per second, and the triaxial magnetometer measures magnetic magnitude and direction for all three axes in units of gauss. Table 1 gives the specifications for each of these MEMS. The "inertial" data output from the IMU is run through the Kalman filter. The resulting AHRS data will be referred to here as "linear". This data transformation will be discussed in detail in subsequent chapters.

Table 1. TSS-DL sensor specifications (from YEI Technologies 2013a).

Sensor	
Orientation range	360° about all axes
Orientation accuracy	±2° for dynamic conditions & all orientations
Orientation resolution	<0.08°
Orientation repeatability	0.085° for all orientations
Accelerometer scale	±2g / ±4g / ±8g selectable
Accelerometer resolution	14 bit
Accelerometer noise density	99µg/√ Hz
Accelerometer sensitivity	0.00024g/digit for ±2g range (±6g range for HH) 0.00048g/digit for ±4g range (±12g range for HH) 0.00096g/digit for ±8g range (±24g range for HH)
Accelerometer temperature sensitivity	±0.008%/°C
Gyro scale	±250/±500/±2000 °/sec selectable
Gyro resolution	16 bit
Gyro noise density	0.03°/sec/√ Hz
Gyro bias stability @ 25°C	11°/hr average for all axes
Gyro sensitivity	0.00875°/sec/digit for ±250°/sec 0.01750°/sec/digit for ±500°/sec 0.070°/sec/digit for ±2000°/sec
Gyro non-linearity	0.2% full-scale
Gyro temperature sensitivity	±0.016%/°C
Compass scale	±1.3 Ga default. Up to ±8.1 Ga available
Compass resolution	12 bit
Compass sensitivity	5 mGa/digit
Compass non-linearity	0.1% full-scale

The purpose for utilizing the TSS-DL onboard the WRD-B is to attempt to gain more precise and reliable surface wave orbital motion data, particularly along the vertical axis, than was achieved with the GT-31 or X6-2. This thesis aims to test the TSS-DL in a controlled, laboratory setting to diagnose the accuracy of its measurements of simulated surface wave orbital motions. In conjunction with the laboratory testing, we apply algorithms to the data collected by the TSS-DL to determine whether we are able to improve the quality and usefulness of the data. Finally we analyze field data collected by WRD-Bs to assess the accuracy of the TSS-DL in a tidal inlet/river mouth region.

III. DATA TRANSFORMATION

A. REFERENCE FRAMES

A reference frame, as used in this context, assigns a set of axes to a three-dimensional space or object. There are two reference frames that must be presented in order to understand how the data collected by the TSS-DL is transformed into meaningful information. The first is the fixed reference frame of Earth; the terrestrial reference frame. In the terrestrial reference frame we assign the positive $\langle x\ y\ z \rangle$ axes to correspond with east, north, and up, respectively. This is an intuitive assignment of axes when picturing an abscissa laid upon the earth's surface with the x axis parallel to the equator (i.e., latitude) and the y axis parallel to the prime meridian (i.e., longitude). The z axis is aligned with the gravitational force; orthogonal to earth's surface. The terrestrial reference frame is denoted with the superscript "t" $\langle x^t y^t z^t \rangle$. The second reference frame is the body reference frame, denoted with the superscript "b" $\langle x^b y^b z^b \rangle$. The body reference frame assigns $\langle x\ y\ z \rangle$ axes to an object, in this case, the TSS-DL. As Figure 12 shows, the positive x axis extends out of the right side of the TSS-DL, the positive y axis extends out of the front of the TSS-DL, and the positive z axis extends out of the top of the TSS-DL. The assignment of axes to the TSS-DL is intended to perfectly align $\langle x^b y^b z^b \rangle$ with $\langle x^t y^t z^t \rangle$ when the TSS-DL's orientation is such that it is sitting flat on the earth's surface with its right side facing east and its front facing north. The instant that the body reference frame and the terrestrial reference frame are no longer perfectly aligned (i.e., the TSS-DL changes orientation), the data collected by the TSS-DL no longer directly corresponds to the terrestrial reference frame, which is the desired reference frame to analyze data in. To transform the data collected by the TSS-DL from body reference frame to terrestrial reference frame we utilize the power of the quaternion.

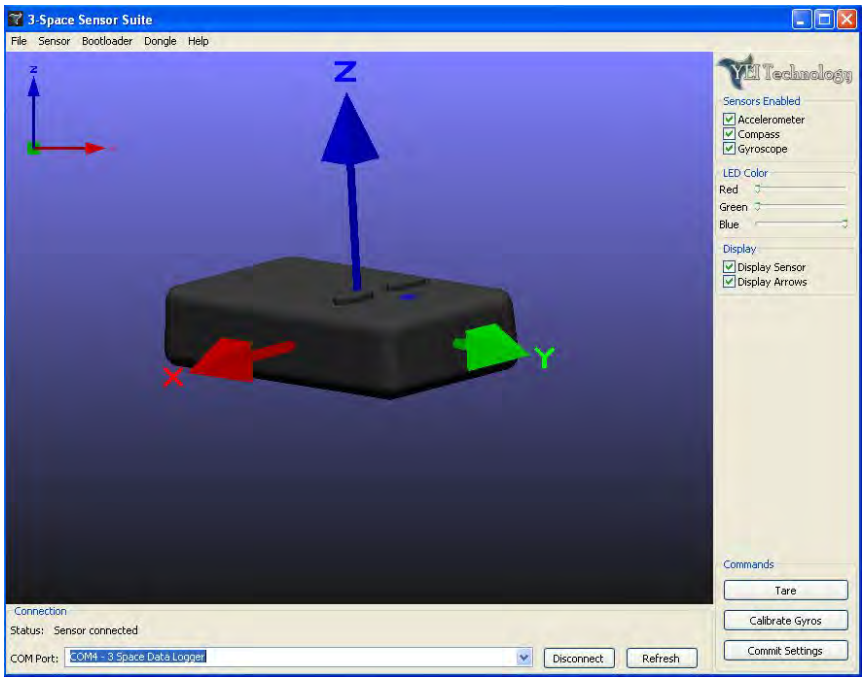

Figure 12. Body reference frame axes assigned to the TSS-DL.

B. QUATERNIONS

To rotate a vector from one reference frame to another requires a so-called quaternion q. Quaternions consist of two parts, a scalar and a vector. The scalar is composed of one real part (q_0) and the vector is composed of three imaginary parts $(q_1 q_2 q_3)$. Here q is represented as a four-element vector (Bachmann 2000).

$$q = [q_0, q_1, q_2, q_3] \tag{1}$$

One of the pieces of data that the TSS-DL records is its own quaternion that is used to transform its data from being body frame referenced to being terrestrial frame referenced. As mentioned before, when the TSS-DL is perfectly oriented on the earth's surface, the body and terrestrial reference frames are the same. As the orientation of the TSS-DL changes though, there is a unique quaternion at each discrete moment in time that exactly describes how the new orientation differs from the terrestrial reference frame.

The TSS-DL's IMU measures inertial accelerations in its body reference frame, so we use the inertial acceleration vector $\vec{a}^b$ in pure quaternion form as the vector we will rotate (Calusdian 2010).

$$\vec{a}^b = \left[0, a_x^b, a_y^b, a_z^b\right] \tag{2}$$

Inertial accelerations must be transformed into the terrestrial reference frame in order for them to have useful meaning to us. Once the inertial accelerations are transformed they are considered linear accelerations and are denoted by $\vec{a}^t$.

In this case q must be a unit quaternion where $|q| = 1$. Along with $\vec{a}^b$ and q, the quaternion conjugate q^* is also required, which is defined as shown (Calusdian 2010).

$$q^* = \left[q_0, -q_1, -q_2, -q_3\right] \tag{3}$$

Using the following operation we are able to transform inertial acceleration data (i.e., body frame referenced) into linear acceleration data (i.e., terrestrial frame referenced) while properly projecting all accelerations onto the correct axes. Details of the quaternion multiplication required for this vector rotation are contained in the Appendix. The evaluation of this equation involves 56 scalar operations, only two trigonometric functions, and produces no singularities (Bachmann 2000).

$$\vec{a}^t = q\vec{a}^b q^* \tag{4}$$

C. ACCELERATION TO DISPLACEMENT

An intuitive way to analyze data in the time domain is by looking at the displacements. By transforming the acceleration data from inertial to linear we are now able to appropriately transform the accelerations into displacements. To do this we perform a double integration of the acceleration data while incorporating a band-pass filter to prevent leakage into our frequency band of interest.

THIS PAGE INTENTIONALLY LEFT BLANK

IV. EXPERIMENTAL DESIGN

In order to validate the TSS-DL for use in surface wave data collection we must first assess its performance in a controlled setting. This requires the ability to simulate surface waves while controlling as many of the variables involved as possible. To accomplish this we constructed a machine to simulate the simplest surface wave motion possible and then conducted tests with the TSS-DL measuring the simulated wave motions.

A. SURFACE WAVE ORBITAL MOTION

The simplest ocean surface waves that exist have a purely sinusoidal form. These are deep water waves, defined by the depth of the water being greater than one half of the wavelength. Assuming such waves have a constant, stationary source and that the waves exist in the absence of any additional influences except for gravity (e.g., currents, winds, rotations, imbalances, etc.), the motion of a particle at the surface traces a circular orbit with the diameter equal to the wave height (see Figure 13).

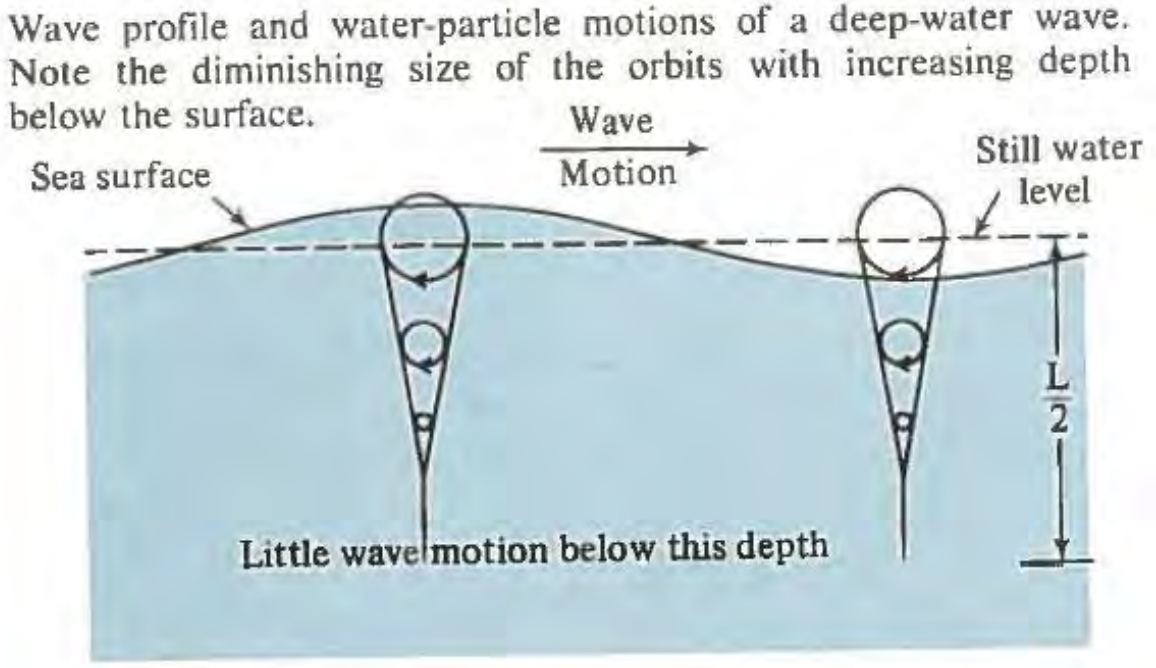

Figure 13. Deep water surface wave orbital motion (from Thurman 1988).

A particle at the surface of the wave field just described experiences accelerations due to both the wave induced pressure variations and the force of gravity. The gravitational force acts to accelerate the particle vertically downward at a rate of $9.81 m/s^2$; however, as the particle is suspended by the surface of the water, it is as though the particle is accelerating upward at the same rate. As waves progress they create pressure variations that also accelerate the particle both vertically and horizontally. At the peak and trough of a wave (i.e., top and bottom of the circular orbit, respectively) the particle experiences maximum vertical acceleration and zero horizontal acceleration. At the equilibrium or still water level the particle experiences maximum horizontal acceleration and zero vertical acceleration. Over one full wave period a plot of the particle's accelerations in time traces a pure sinusoid, with the vertical component also containing the gravitational acceleration constant (i.e., $9.81 m/s^2$).

B. SURFACE WAVE ORBITAL MOTION SIMULATOR

The objective of the surface wave orbital motion simulator (SWOMS) is to allow the TSS-DL to experience controlled surface wave orbital motion. While brainstorming designs for the SWOMS we considered the Ferris wheel (see Figure 14). The Ferris wheel has a central rotational axis and cradles affixed to the ends its arms. The cradles, along with their payload, experience a circular orbit as the Ferris wheel rotates and, of equal importance, they maintain approximately the same orientation throughout the orbit. The speed of rotation of a Ferris wheel can be controlled and varied. With the Ferris wheel framework in mind we set out to build the SWOMS.

Figure 14. Ferris wheel (from Free Wallpapers 2013).

To simplify the construction of the SWOMS we use a single arm bisected by a rotational shaft. For the arm we use a 0.5” x 1.25” redwood board cut to 1.1m in length. At 0.55m we drilled a hole through the 1.25” width to insert and secure a rotational shaft (see Figure 15).

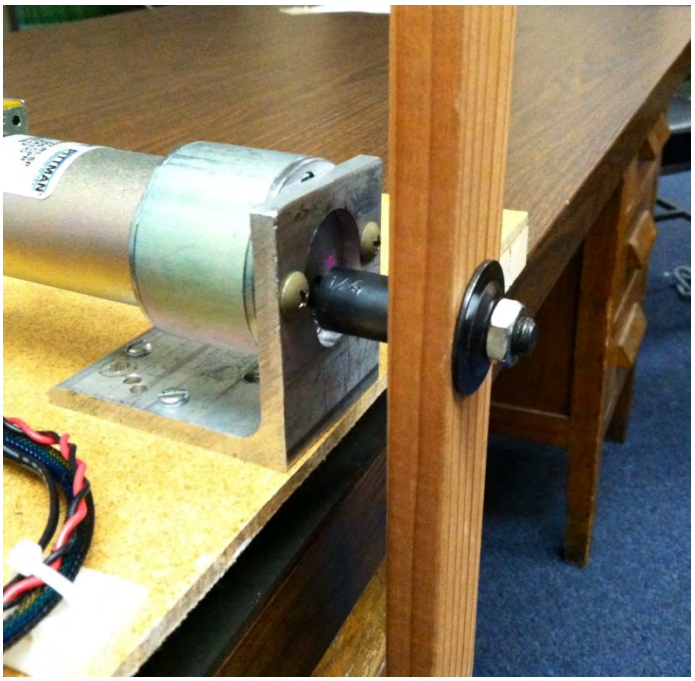

Figure 15. SWOMS rotational arm secured to motor shaft.

The rotational shaft is that of a Pittman series GM9000 lo-cog brush commutated DC gearmotor (see Figure 16).

Figure 16. SWOMS Pittman DC motor.

The motor is powered by a plug and a standard 120V/60Hz U.S. power outlet. The motor control wires connect to a Solutions Cubed Motion Mind 3 DC motor motion controller (see Figure 17).

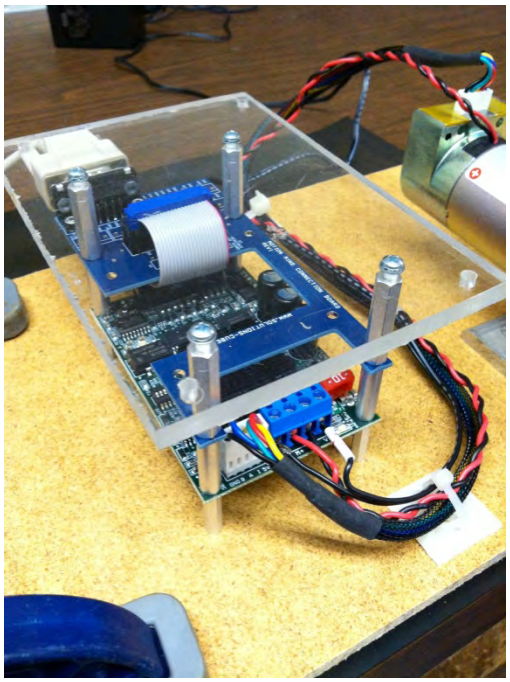

Figure 17. SWOMS Motion Mind 3 motor controller.

To interface with the Win7 Motion Mind 3 ASCII Control Software we connect the Motion Mind 3 to a desktop computer via serial cable. From the software's graphical user interface (GUI) we are able to select inputs to control the precise rate of rotation of the SWOMS (see Figure 18).

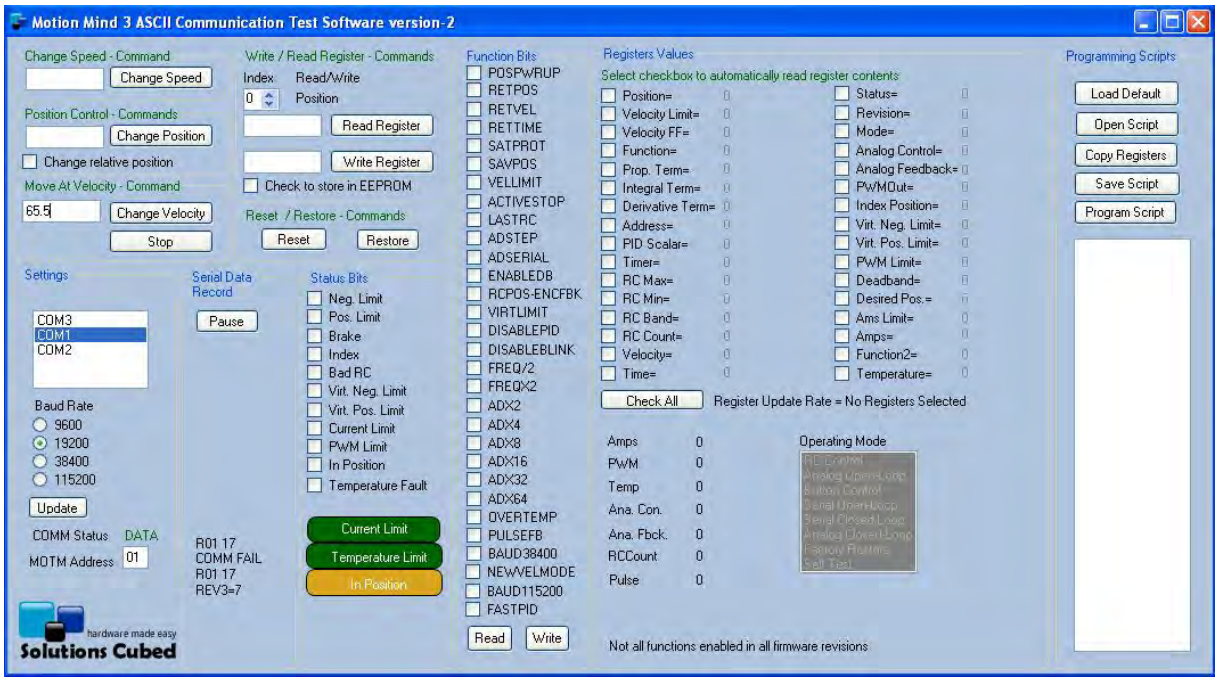

Figure 18. Motion Mind 3 GUI.

Built into the software is the following equation to convert a velocity input to a rotational frequency for a given motor (Solutions Cubed 2013b):

$$V = \frac{f \times C\ P\ R \times G\ R}{5\ 0} \tag{5}$$

Here V is the GUI velocity input, f is the rotational frequency (i.e., motor shaft rotations per second), CPR is the counts per revolution defined by the specific motor being used, and GR is the gear ratio also defined by the specific motor being used. For our Pittman motor the CPR is 500 and the GR is 65.5:1. For ease of use we generate a spreadsheet utilizing this algorithm to automatically convert desired frequencies into GUI velocity inputs. Now that we have a precisely controllable rotational arm that at each point on the arm experiences circular orbit, we set out to create a method for attaching the TSS-DL to the arm.

Just as Ferris wheel cradles maintain roughly a single orientation throughout their full circular orbit, so too should the TSS-DL and its cradle maintain a single orientation throughout its orbit to avoid the introduction of additional accelerations beyond those

previously mentioned. Two identical cradles are created for the SWOMS, one mounted at each end of the rotational arm. In considering the cradle components, we strive to avoid the use of magnetic materials (e.g., iron and conventional steel) as they can disrupt the measurements made by the TSS-DL's magnetometers. Additionally we aim to keep the overall weight of the cradle low to reduce stress on the motor. For the cradle's main arm we use a 4" long, 0.5" diameter fully threaded aluminum screw. A hole is drilled through the SWOMS's main rotational arm at exactly 0.05m from the end of the arm, placing it exactly 0.5m from the SWOMS's axis of rotation, which ultimately creates a simulated wave height of 1m. We insert the aluminum screw through this hole and secure it with aluminum washers and nuts, which create the backbone for the cradle (see Figure 19). Acetal ball bearings with glass balls are fed onto the aluminum screw to as nearly as possible eliminate the transfer of the rotational motion from the SWOMS's rotational arm to the cradle and TSS-DL, thereby enabling the cradle and TSS-DL to maintain a single orientation throughout the orbit. On the bearings we mount approximately a 2" long section of 0.75" thick, medium-softness polyurethane tubing.

Figure 19. SWOMS cradle arm, hardware, bearing, and tubing.

Using small stainless-steel screws we secure two 4.75” long, 0.5” wide aluminum stanchions to opposite sides of the polyurethane tubing (see Figure 20). An additional third aluminum stanchion is mounted orthogonal to the others and beneath the platform to provide increased support and rigidity

Figure 20. SWOMS cradle stanchions.

Between these stanchions we secure a 3” long by 2” wide wooden platform upon which the TSS-DL will be mounted during testing (see Figure 21).

Figure 21. SWOMS cradle platform.

In order for the bearings to function properly in maintaining a single orientation for the TSS-DL's cradle, we add a small amount of ballast weight to the underside of the cradle. The weight is provided by 15 0.375" stainless-steel hex nuts looped onto a 0.25" wide zip-tie (see Figure 22). The rigidity of the zip-tie helps to significantly reduce a pendulum-like oscillation of the ballast weight once the SWOMS is in motion.

Figure 22. SWOMS ballast weight.

A platform of 0.25”-thick fiberboard approximately 8”-wide by 16”-long mounted atop two 8”-long, 2.5”-wide, 0.75”-thick boards at either end of the fiberboard serve as the foundation of the SWOMS. On the top of the platform is mounted the Motion Mind 3 circuitry, the Pittman motor, and the associated wiring. The motor is mounted near the centerline of the platform via an aluminum bracket and oriented such that the rotational shaft of the motor extends out beyond the edge of the platform, which provides the clearance for the SWOMS main rotational arm.

For the testing we mount the SWOMS platform on the corner of a sturdy wooden desk and secure it with clamps. Ideally we would create a stand-alone structure specifically for the SWOMS that is both sturdy and stationary for testing, yet mobile enough that the SWOMS can be easily reoriented or relocated. Testing is conducted in one of the ocean laboratories at NPS. The SWOMS is in close enough proximity that we are able to connect the Motion Mind 3 to a desktop computer via a 6’ serial cable (see Figure 23).

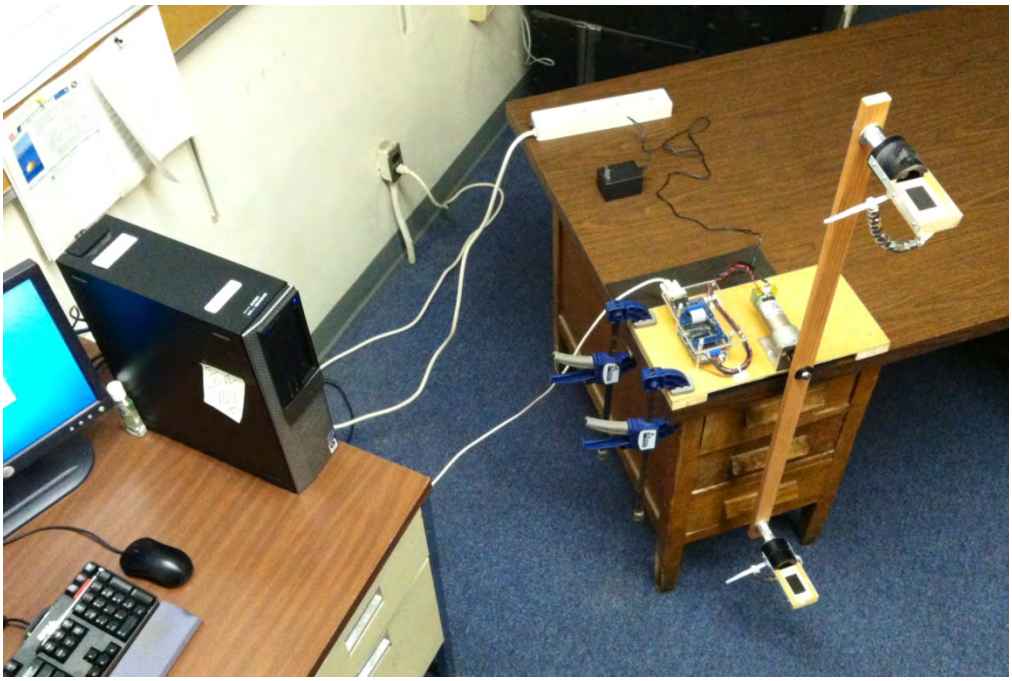

Figure 23. SWOMS setup in the laboratory.

THIS PAGE INTENTIONALLY LEFT BLANK

V. TESTS AND RESULTS

A. OVERVIEW OF TESTS

1. Test Configurations

We designed three types of tests to assess the performance of the TSS-DL. The first test we refer to as the optimal orientation test, or simply "optimal." In the optimal testing configuration the SWOMS is oriented such that the axis of the rotating arm is aligned as nearly as possible with the magnetic north-south axis to allow rotation of the arm and sensor package only in the east-west and vertical planes. Additionally, the ballast weight that was discussed earlier is in place to maintain the horizontal orientation of the TSS-DL. The purpose of the optimal testing configuration is to align the TSS-DL's body reference frame with the terrestrial reference frame. By doing so we are able to assess both the inertial data as well as the linear data from the TSS-DL, which should correspond to each other fairly well, particularly in the vertical.

The second test we refer to as the skewed orientation test, or simple "skewed." In the skewed testing configuration the SWOMS is oriented at a random angle such that the rotating arm and TSS-DL are now rotating in the entire three-dimensional (i.e., east-west, north-south, and vertical) space. Ballast weights remain in place just as they are in the optimal tests. The purpose of the skewed testing configuration is to remove the near perfect alignment of the TSS-DL's body reference frame with the terrestrial reference frame. By doing this while keeping all other variables constant, we are able to assess how well the TSS-DL is able to resolve the horizontal motions.

The third test we refer to as the altered ballast test, or simple "AB." In the AB testing configuration the SWOMS is oriented at the same random angle as in the skewed tests, but now we remove the ballast weight from the cradles and allow the TSS-DL to experience random and extreme changes to its horizontal orientation. By doing this we are able to assess how well the TSS-DL is able to resolve large pitch/roll angles, such as those experienced in breaking ocean waves.

2. Test Specifications

Tests were conducted for all three testing configurations at 0.07Hz, 0.1Hz, 0.2Hz, 0.3Hz, and 0.4Hz. These frequencies were chosen to correspond to the dominant swell (i.e., 0.05–0.15Hz) and wind-sea (i.e., 0.15–0.3Hz) frequency bands, as well as the frequency range examined in previous field studies by Herbers et al. (2012) and Pearman et al. (2013). The 0.05Hz frequency was initially tested; however, we discovered that the system noise at that frequency and below made it nearly impossible to detect the slow circular rotation signal in the noise. The 0.4Hz frequency is tested to see the results of a 1m wave nearing its limit of steepness before breaking. All tests were run for a duration of approximately 15 minutes with the TSS-DL sampling at a rate of 10Hz. All records were truncated such that the first full minute of the record (i.e., 600 sample points) was eliminated, as well as a portion of the end of the record such that the total record length for every test was exactly 8192 (i.e., 2^{13}) data points, or approximately 13.65 minutes. This record length was chosen to allow for a robust sampling of the test frequency and to yield a sufficiently high frequency resolution in the spectra.

B. OVERVIEW OF DATA

1. Data Types

For every test we evaluated the TSS-DL's performance by comparing measured accelerations with the known circular motion of the SWOMS. Vertical and horizontal components of acceleration A are purely sinusoidal oscillations with amplitudes equal to the length of the radial arm R, which is 0.5m, multiplied by ω^2 with the frequency of oscillation ω equal to the frequency of our given test (i.e., 0.07Hz, 0.1Hz, etc.) and phase φ of the vertical and horizontal accelerations differing by 90 degrees.

$$A = -R \times \omega^2 \times \cos(\omega \times t + \varphi) \tag{6}$$

This analytic data serves as our control data for a constant, purely circular motion in the absence of noise.

The second type of data is the inertial acceleration data recorded by the TSS-DL. This data is TSS-DL body frame referenced and is strictly the measurements made by the

TSS-DL, with the only modification being the removal of gravity from the z-axis. This modification was implemented to more closely compare the inertial and linear results in the optimal and skewed tests; however, in the AB tests with extreme angles, large gravity contributions remain in the data. In order to maintain consistent techniques among all tests, this modification is used for all tests.

The third type of data is the linear acceleration data recorded by the TSS-DL. This data is the inertial data that has been transformed into linear data (i.e., terrestrial frame referenced and gravity removed) through the use of Equation (4).

2. Data Parameters

For each type of data, four parameters are calculated to ultimately assess the performance of the TSS-DL. The parameters assessed are the total variance σ^2_{tot}, signal variance σ^2_{sig} in the frequency band containing the circular motion, signal amplitude a_{sig}, and signal to noise ratio SNR of the signal variance to total variance. Variance σ^2 is defined as the area (i.e., energy) under the spectral curve of a power spectral density (PSD) function $G(f)$

$$\sigma^2 = \int_0^{f_n} G(f)df \tag{7}$$

All parameters are calculated from the PSD, which is computed using MATLAB's cross power spectral density (CPSD) function with the analytic, inertial, or linear accelerations as the input time series, each with a length of 8192 points. Default parameters were utilized in this function, which divide the record into window lengths of 2048 points using Hamming windows and with 50% overlap. This yields a frequency resolution Δf of 0.0049Hz for each of the PSDs. Each PSD is calculated for the frequency range of 0.03–1.0Hz. This is done in order to exclude the significant amount of system noise present in the very low frequency range (i.e., <0.03Hz) and higher frequencies where the WRDs do not yield usable data.

Once a PSD was computed, the energy under the spectral curve and bounded by 0.03Hz and 1.0Hz was calculated, which gives σ_{tot}^2. The signal in the spectrum of a given test was defined by the peak centered on the input frequency, and including three neighboring bands on both sides of the peak. The energy under this peak gives σ_{sig}^2. The amplitude of the signal was computed using the following equation

$$a_{sig} = \sqrt{2 \times \sigma_{sig}^2} \tag{8}$$

The SNR was computed using the following equation

$$SNR = \frac{\sigma_{sig}^2}{\sigma_{tot}^2} \tag{9}$$

C. OPTIMAL TEST CASE

To illustrate the results from a test, we will step through an optimal test run at 0.2Hz using TSS-DL 18F.

1. Accelerations

Figures 24–26 show the plots of the analytic, inertial, and linear accelerations plotted against time for the z, x, and y axes, respectively.

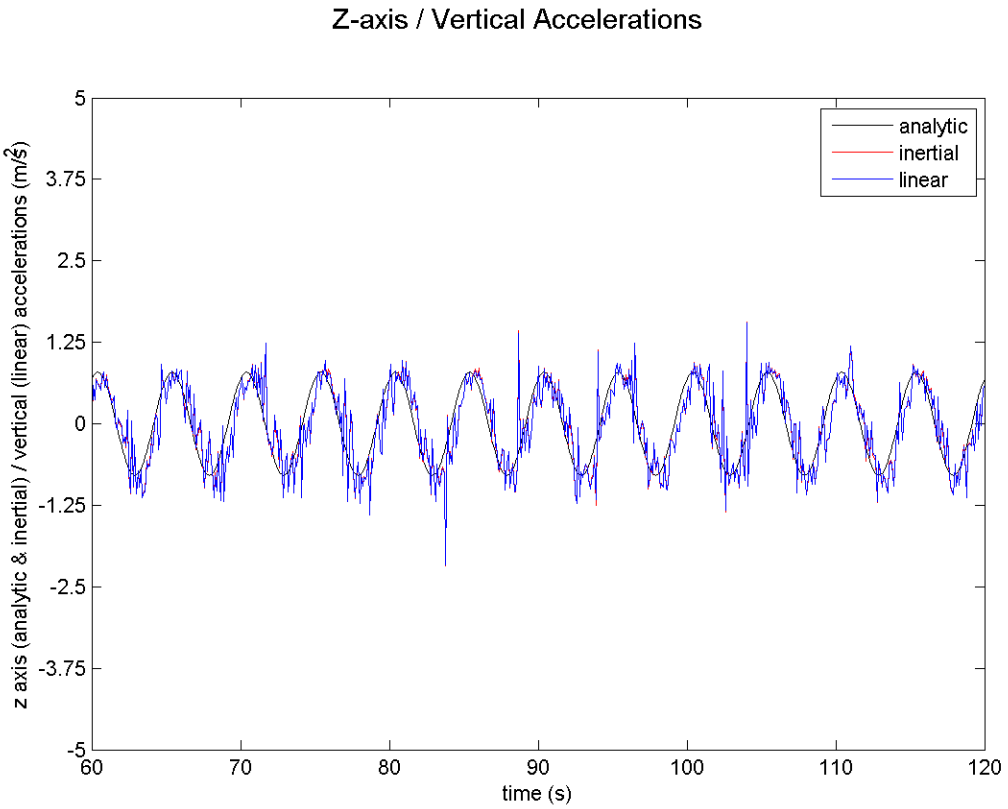

Figure 24. z-axis / vertical accelerations from TSS-DL 18F for optimal test at 0.2Hz.

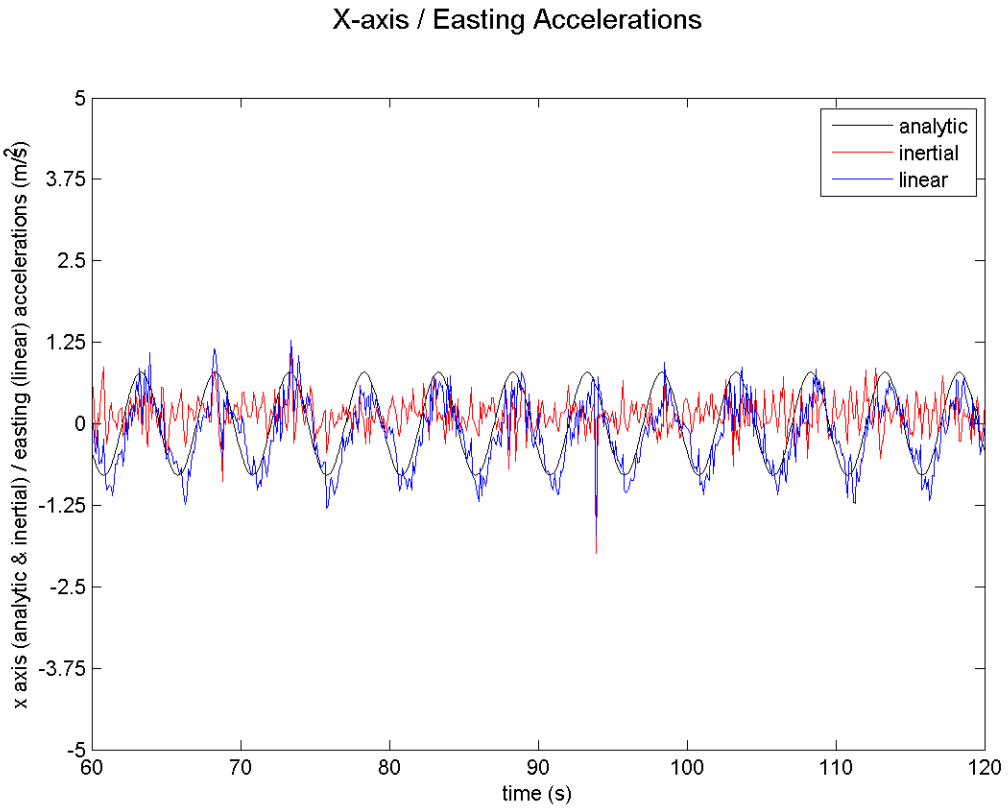

Figure 25. x-axis / easting accelerations from TSS-DL 18F for optimal test at 0.2Hz.

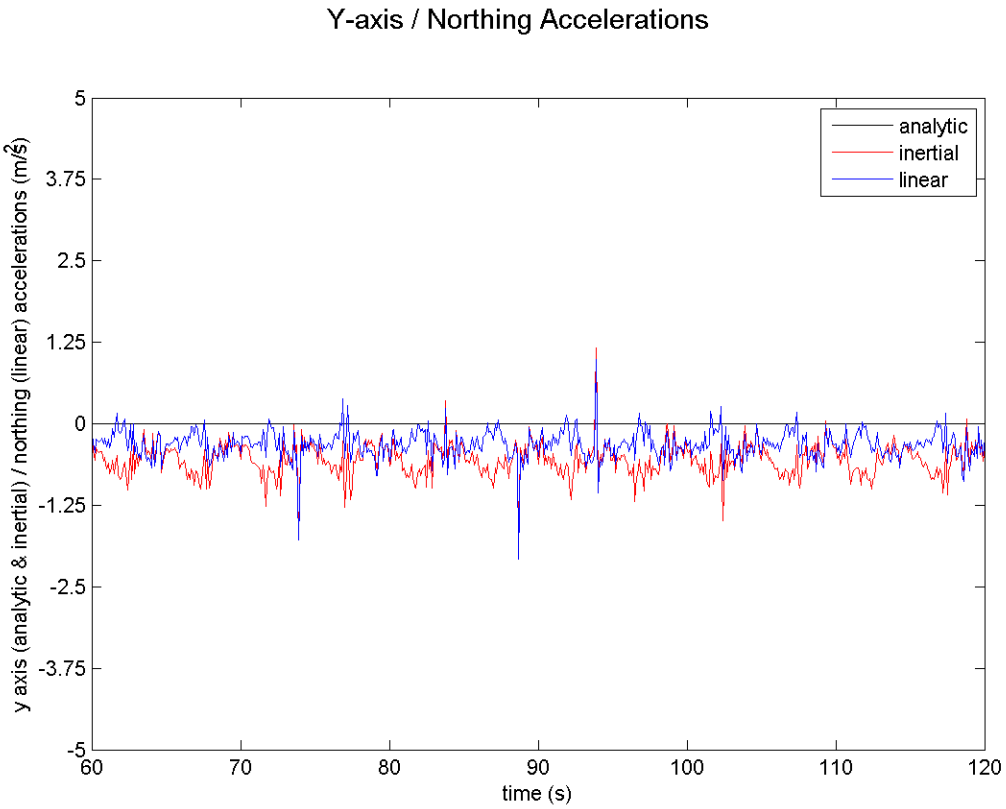

Figure 26. y-axis / northing accelerations from TSS-DL 18F for optimal test at 0.2Hz.

The plot of z-axis / vertical accelerations (see Figure 24) is representative of what we might expect to see. The analytic accelerations trace a sinusoid with a 5s period and an amplitude of 0.7894m/s^2. The inertial and linear accelerations also both trace sinusoids with a 5s period, but with system noise present in the signal. The inertial and linear accelerations are in close agreement, which indicates that the pitch/roll contributions to the vertical inertial accelerations are negligible. This confirms that the SWOMS maintains the horizontal orientation of the TSS-DL during the optimal tests. It also confirms that the TSS-DL accurately resolves the accelerations of the circular motion.

The plot of x-axis / easting accelerations (see Figure 25) shows, as expected, analytic accelerations identical to the z-axis accelerations, phase shifted by 90 degrees. Here the inertial x-axis accelerations have no clearly identifiable sinusoidal pattern to

them and appear to be dominated by noise. This can be attributed to multiple factors including contamination from gravity and system noise. The easting linear accelerations on the other hand show a distinct sinusoid pattern that mirrors the analytic accelerations while also containing system noise and slight deviations in the amplitude. This confirms that the algorithm transforming the inertial accelerations into linear accelerations is working correctly. It also confirms that the SWOMS is oriented well for optimal tests.

In the plot of y-axis / northing accelerations (see Figure 26) the analytic acceleration vanishes. The inertial y-axis accelerations show minimal noise present on a small sinusoidal pattern. The northing linear accelerations also show a similar pattern with even less of a sinusoidal signature. By comparing these accelerations to the x-axis / easting accelerations we see that there is a relatively small amount of acceleration occurring along the y-axis / northing direction that is likely the result of coherent system noise, minor sensor calibration error, and/or a slight misalignment of the SWOMS to the terrestrial reference frame.

2. Power Spectral Density of Accelerations

Figures 27 and 28 show the PSD of analytic, inertial, and linear accelerations for the vertical and horizontal axes, respectively.

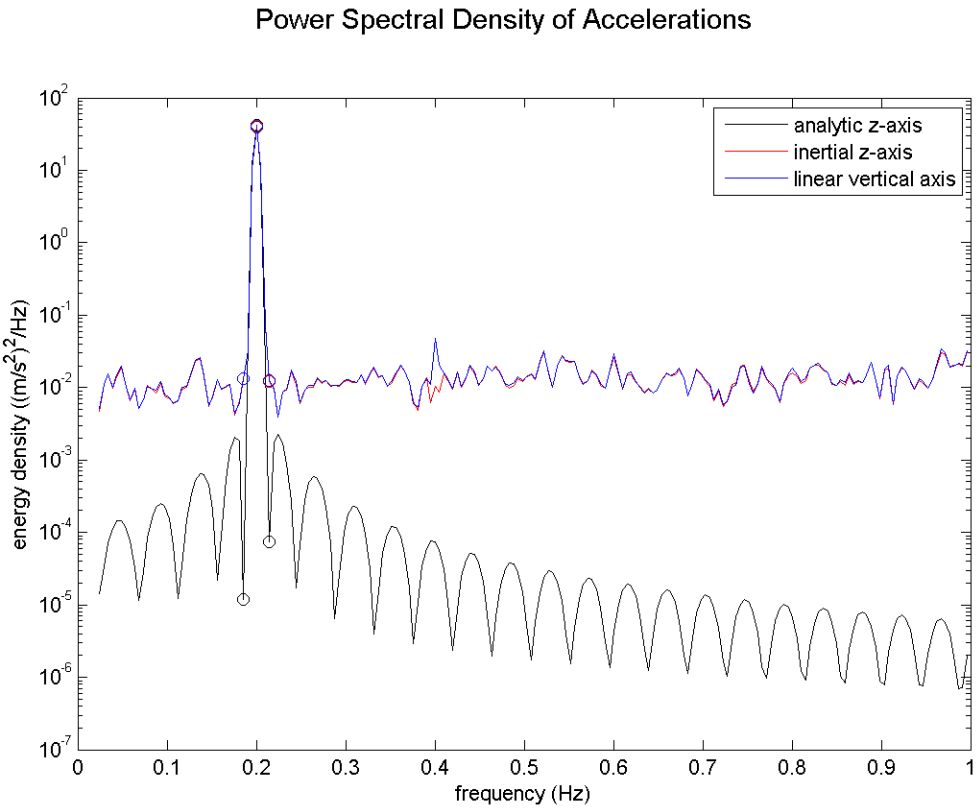

Figure 27. PSD of z-axis / vertical accelerations from TSS-DL 18F for optimal test at 0.2Hz.

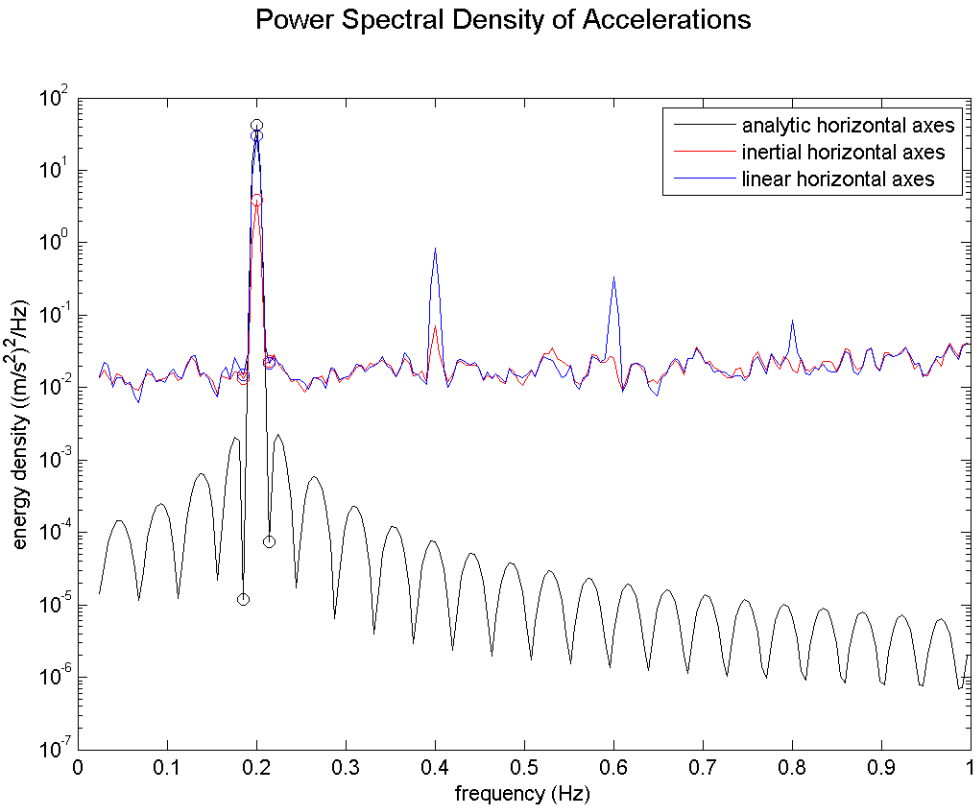

Figure 28. PSD of horizontal axes accelerations from TSS-DL 18F for optimal test at 0.2Hz.

The PSD of z-axis / vertical accelerations (see Figure 27) shows energy density spread across the frequency spectrum, with the area under the spectral curve representing the variance. The energy density of the analytic accelerations is much lower than that of either the inertial or linear accelerations because the analytic accelerations contain no noise. The signal in the spectral curve for all three vertical accelerations is centered over 0.2Hz, which corresponds to the frequency of the test. The amplitude of that signal for the analytic accelerations corresponds to the amplitude seen in the acceleration versus time plots, which is 0.7894m/s^2. The total and signal variances under the spectral curve of analytic accelerations are 63.8371m^2/s^4 and 63.8134m^2/s^4, respectively, yielding a SNR of 0.9996. The spectral curves of the inertial and linear accelerations are nearly identical to each other, similar to the acceleration versus time plots. Further, the signal peaks in all three spectral curves collapse nearly perfectly, with the only major difference

between them being the noise present in the inertial and linear accelerations. The signal amplitudes of the inertial and linear acceleration spectra are 0.7797m/s^2 and 0.7737m/s^2, respectively, putting them in excellent agreement with the analytic amplitude. The total and signal variances under the spectral curve of inertial accelerations are 64.8159m^2/s^4 and 62.2586m^2/s^4, respectively, yielding a SNR of 0.9605. The total and signal variances under the spectral curve of linear accelerations are 63.9776m^2/s^4 and 61.3020m^2/s^4, respectively, yielding a SNR of 0.9582. While there is noise present in the inertial and linear accelerations, for optimal tests the raw TSS-DL data accurately resolves the vertical component of the signal.

The PSD of horizontal axes accelerations (see Figure 28) shows similar results to those seen in the PSD of vertical accelerations. The major difference in this PSD is the amplitude of the energy density signal from the different accelerations, and to a lesser extent, the presence of smaller spikes at the harmonics of the primary frequency. The values associated with the spectral curve of analytic accelerations remain the same. The signal amplitudes for the inertial and linear acceleration spectral curves are 0.2437m/s^2 and 0.6660m/s^2, respectively. The total and signal variances under the spectral curve of inertial accelerations are 9.8634m^2/s^4 and 6.0835m^2/s^4, respectively, yielding a SNR of 0.6168. The total and signal variances under the spectral curve of linear accelerations are 50.8772m^2/s^4 and 45.4205m^2/s^4, respectively, yielding a SNR of 0.8927. This tells us that there is good agreement between the linear and analytic accelerations as indicated by the signal amplitude and SNR. The agreement between the inertial and analytic accelerations is poor, similar to the results in the time domain. The poor agreement between inertial and analytic accelerations here makes sense as the inertial accelerations are body frame referenced while the analytic accelerations are terrestrial frame referenced.

3. Displacements

Analytic displacements d were generated using the following equation where again the phase φ of horizontal and vertical components differ by 90 degrees.

$$d = a \times \cos(\omega \times t + \varphi) \tag{10}$$

Displacements from the inertial and linear accelerations were calculated using the method described in Chapter III C. Figures 29 and 30 show the displacements calculated from analytic, inertial, and linear accelerations and plotted against time for both the vertical and horizontal (i.e., east-west) axes, respectively in the plane of the circular motion.

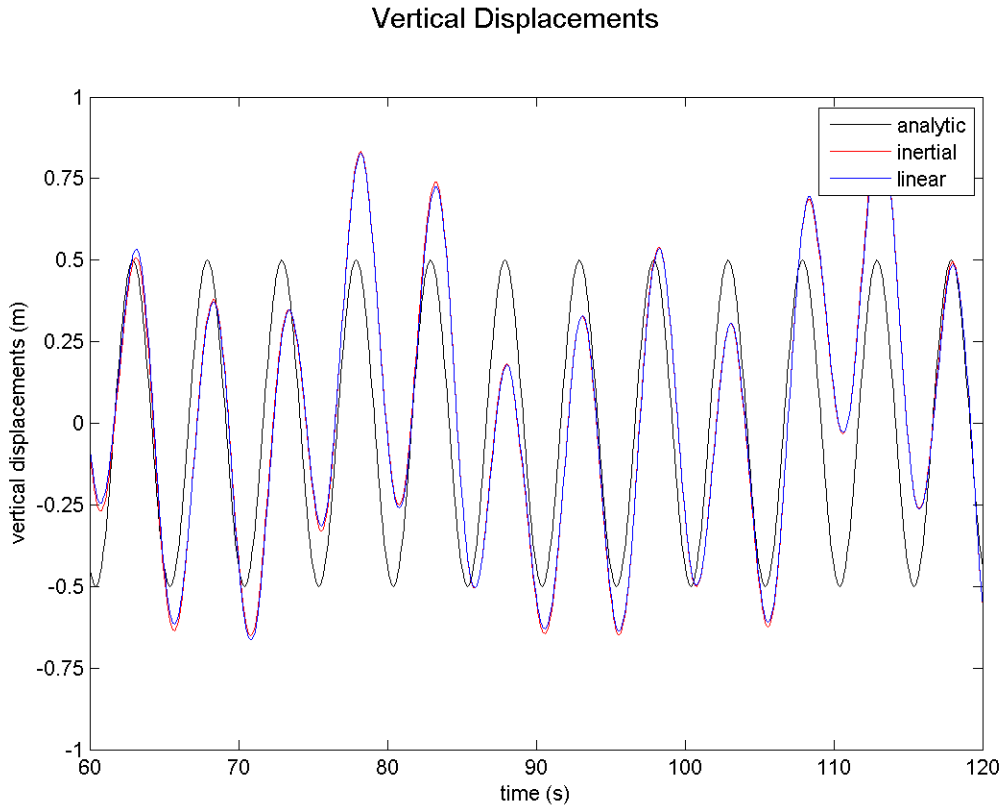

Figure 29. Vertical displacements from TSS-DL 18F for optimal test at 0.2Hz.

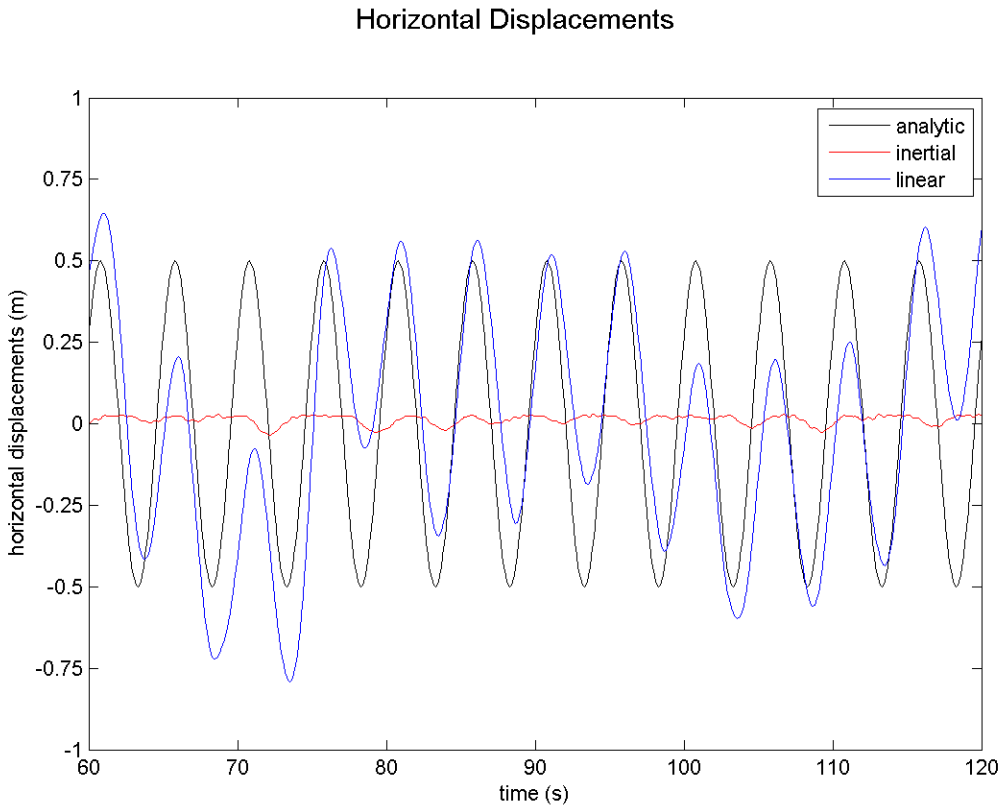

Figure 30. Horizontal displacements from TSS-DL 18F for optimal test at 0.2Hz.

The vertical displacements plot (see Figure 29) shows that the analytic displacements trace a sinusoid with a 5s period and 0.5m amplitude, which is expected and corresponds well with the vertical analytic solution. The inertial and linear displacements are nearly identical to each other, which is expected given that the accelerations from which the displacements were derived were nearly identical. This further confirms that the TSS-DL can accurately resolve the simulated vertical wave excursions in the optimal tests.

The horizontal displacements plot (see Figure 30) shows good agreement between the linear and analytic displacements; however, the inertial displacements have no discernable pattern to them. This further confirms that the TSS-DL can resolve horizontal motions in a seemingly incoherent dataset after the quaternion transformation is applied.

D. RESULTS

The tables in this section document the complete results of their respective tests. Analytic data is shown for comparison. Inertial data is shown to exhibit the degree to which this data improves when transformed to linear data. Linear data is the true measure of the performance of the TSS-DL.

1. Optimal Tests

Table 2 shows the results from the optimal tests. The linear SNRs trend from lower values at lower frequencies to higher values at higher frequencies. This trend can be attributed to weaker acceleration signals (for fixed displacement amplitude) as the frequency is reduced, whereas the noise extends across the entire spectrum, thus degrading the SNR. The linear vertical signal amplitudes show excellent agreement to the analytic signal amplitudes throughout the spectrum tested, with the average difference between them across all optimal tests being $\pm 3\%$. The linear horizontal signal amplitudes show excellent agreement at and above 0.3Hz, but decreasing agreement with decreasing frequency below 0.3Hz, with the average difference between them across all optimal tests being $\pm 21\%$.

Table 2. Optimal test data.

Optimal

		Analytic			
Freq (Hz)	TSS-DL	σ^2_{tot}	σ^2_{sig}	a_{sig}	SNR
0.07	N/A	0.0047	0.0047	0.0967	0.9997
0.1	N/A	0.0195	0.0195	0.1974	0.9997
0.2	N/A	0.3128	0.3127	0.7894	0.9996
0.3	N/A	1.5836	1.5831	1.7763	0.9997
0.4	N/A	5.0049	5.0029	3.1577	0.9996

		Inertial Vertical				Linear Vertical				
Freq (Hz)	TSS-DL	σ^2_{tot}	σ^2_{sig}	a_{sig}	SNR	σ^2_{tot}	σ^2_{sig}	a_{sig}	SNR	a_{sig} % diff from analytic
0.07	18B	0.0102	0.0049	0.0985	0.4764	0.0110	0.0055	0.1051	0.5024	0.0799
0.07	192	0.0093	0.0042	0.0917	0.4525	0.0103	0.0050	0.0999	0.4884	0.0320
0.1	18B	0.0257	0.0190	0.1946	0.7384	0.0260	0.0190	0.1944	0.7297	-0.0154
0.1	192	0.0258	0.0179	0.1891	0.6953	0.0262	0.0180	0.1896	0.6891	-0.0411
0.2	18E	0.3339	0.3134	0.7904	0.9388	0.3274	0.3061	0.7811	0.9350	-0.0106
0.2	18F	0.3176	0.3051	0.7797	0.9605	0.3135	0.3004	0.7737	0.9582	-0.0203
0.3	18E	1.6407	1.5797	1.7744	0.9628	1.6058	1.5399	1.7518	0.9590	-0.0140
0.3	18F	1.5238	1.4952	1.7262	0.9812	1.5124	1.4765	1.7154	0.9762	-0.0355
0.4	18B	4.5742	4.5141	2.9994	0.9869	4.6339	4.5640	3.0160	0.9849	-0.0470
0.4	192	4.7343	4.6825	3.0548	0.9891	4.5383	4.4558	2.9800	0.9818	-0.0596

		Inertial Horizontal				Linear Horizontal				
Freq (Hz)	TSS-DL	σ^2_{tot}	σ^2_{sig}	a_{sig}	SNR	σ^2_{tot}	σ^2_{sig}	a_{sig}	SNR	a_{sig} % diff from analytic
0.07	18B	0.0270	0.0145	0.1698	0.5364	0.0511	0.0353	0.2653	0.6903	0.6355
0.07	192	0.0406	0.0291	0.2409	0.7174	0.0478	0.0316	0.2509	0.6609	0.6146
0.1	18B	0.0260	0.0119	0.1540	0.4573	0.0573	0.0397	0.2813	0.6933	0.2983
0.1	192	0.0392	0.0298	0.2436	0.7598	0.0494	0.0357	0.2668	0.7228	0.2601
0.2	18E	0.0428	0.0143	0.1687	0.3339	0.2890	0.2570	0.7157	0.8892	-0.1030
0.2	18F	0.0483	0.0298	0.2437	0.6168	0.2493	0.2226	0.6660	0.8927	-0.1853
0.3	18E	0.0857	0.0388	0.2781	0.4528	1.6414	1.5532	1.7594	0.9463	-0.0096
0.3	18F	0.0698	0.0155	0.1757	0.2220	1.7230	1.6415	1.8087	0.9527	0.0179
0.4	18B	0.1543	0.0711	0.3763	0.4607	4.9809	4.9103	3.1283	0.9859	-0.0094
0.4	192	0.1231	0.0717	0.3781	0.5829	5.1876	5.1073	3.1904	0.9845	0.0102

2. Skewed Tests

Table 3 shows the results from the skewed tests. Similar to the optimal tests results, these results demonstrate excellent agreement between the linear vertical signal amplitudes and analytic signal amplitudes, with the average difference between them across all skewed tests being $\pm$ 4%. Once more we see the trend of lower SNR values at lower frequencies to higher SNR values at higher frequencies. We also see decreasing agreement between the linear horizontal signal amplitudes and analytic signal amplitudes

with decreasing frequency, with the average difference between them across all skewed tests being $\pm 25\%$. These tests demonstrate that the transformation algorithm can be applied to an arbitrary horizontal orientation of the TSS-DL.

Table 3. Skewed test data.

Skewed										
		Analytic								
Freq (Hz)	TSS-DL	σ^2_{tot}	σ^2_{sig}	a_{sig}	SNR					
0.07	N/A	0.0047	0.0047	0.0967	0.9997					
0.1	N/A	0.0195	0.0195	0.1974	0.9997					
0.2	N/A	0.3128	0.3127	0.7894	0.9996					
0.3	N/A	1.5836	1.5831	1.7763	0.9997					
0.4	N/A	5.0049	5.0029	3.1577	0.9996					
		Inertial Vertical				Linear Vertical				
Freq (Hz)	TSS-DL	σ^2_{tot}	σ^2_{sig}	a_{sig}	SNR	σ^2_{tot}	σ^2_{sig}	a_{sig}	SNR	a_{sig} % diff from analytic
0.07	18B	0.0106	0.0049	0.0988	0.4607	0.0115	0.0056	0.1056	0.4856	0.0843
0.07	192	0.0106	0.0046	0.0955	0.4303	0.0117	0.0055	0.1044	0.4694	0.0738
0.1	18E	0.0262	0.0204	0.2016	0.7793	0.0272	0.0212	0.2056	0.7784	0.0399
0.1	18F	0.0235	0.0187	0.1929	0.7957	0.0241	0.0191	0.1953	0.7953	-0.0108
0.2	18E	0.3209	0.3095	0.7853	0.9643	0.3167	0.3045	0.7790	0.9614	-0.0134
0.2	18F	0.3216	0.3065	0.7816	0.9531	0.3173	0.3014	0.7750	0.9500	-0.0186
0.3	18E	1.6350	1.5865	1.7782	0.9703	1.6215	1.5722	1.7701	0.9696	-0.0035
0.3	18F	1.5203	1.4896	1.7230	0.9798	1.5029	1.4683	1.7106	0.9770	-0.0384
0.4	18B	4.5910	4.5317	3.0053	0.9871	4.5729	4.5176	3.0006	0.9879	-0.0524
0.4	192	4.7116	4.6582	3.0469	0.9887	4.5692	4.5145	2.9996	0.9880	-0.0527
		Inertial Horizontal				Linear Horizontal				
Freq (Hz)	TSS-DL	σ^2_{tot}	σ^2_{sig}	a_{sig}	SNR	σ^2_{tot}	σ^2_{sig}	a_{sig}	SNR	a_{sig} % diff from analytic
0.07	18B	0.0379	0.0250	0.2234	0.6609	0.0425	0.0255	0.2255	0.6009	0.5712
0.07	192	0.0179	0.0037	0.0853	0.2044	0.0428	0.0250	0.2231	0.5837	0.5666
0.1	18E	0.0312	0.0240	0.2188	0.7690	0.0438	0.0311	0.2488	0.7099	0.2066
0.1	18F	0.0235	0.0066	0.1151	0.2825	0.0505	0.0305	0.2464	0.6029	0.1989
0.2	18E	0.0428	0.0262	0.2287	0.6127	0.2056	0.1801	0.5992	0.8760	-0.3174
0.2	18F	0.0363	0.0066	0.1143	0.1807	0.2175	0.1891	0.6139	0.8695	-0.2859
0.3	18E	0.0802	0.0375	0.2733	0.4674	1.3113	1.2522	1.5797	0.9549	-0.1245
0.3	18F	0.0878	0.0272	0.2330	0.3101	1.3590	1.2928	1.6052	0.9513	-0.1066
0.4	18B	0.1468	0.0508	0.3180	0.3457	4.4669	4.4016	2.9618	0.9854	-0.0661
0.4	192	0.1260	0.0665	0.3640	0.5278	4.5484	4.4854	2.9899	0.9862	-0.0561

3. AB Tests

Table 4 shows the results from the AB tests. These tests created extreme conditions unlikely to be seen in real world ocean conditions. The tests with the TSS-DL highlighted by an asterisk indicate that during these tests the TSS-DL's cradle never righted itself during the rotations, thereby fixing the TSS-DL in a single orientation and

causing it to invert during each rotation. Even under these conditions the linear vertical signal amplitudes show strong overall agreement to the analytic signal amplitudes, with the average difference between them across all AB tests being $\pm 7\%$. Once more the linear horizontal signal amplitudes show decreasing agreement to the analytic signal amplitudes with decreasing frequency, with the average difference between them across all AB tests being $\pm 33\%$. SNRs continue to show the trend seen in the optimal and skewed tests.

Table 4. AB test data.

AB

		Analytic			
Freq (Hz)	TSS-DL	σ^2_{tot}	σ^2_{sig}	a_{sig}	SNR
0.07	N/A	0.0047	0.0047	0.0967	0.9997
0.1	N/A	0.0195	0.0195	0.1974	0.9997
0.2	N/A	0.3128	0.3127	0.7894	0.9996
0.3	N/A	1.5836	1.5831	1.7763	0.9997
0.4	N/A	5.0049	5.0029	3.1577	0.9996

		Inertial Vertical				Linear Vertical				
Freq (Hz)	TSS-DL	σ^2_{tot}	σ^2_{sig}	a_{sig}	SNR	σ^2_{tot}	σ^2_{sig}	a_{sig}	SNR	a_{sig} % diff from analytic
0.07	18E	5.7977	1.1723	1.5285	0.2022	0.0200	0.0072	0.1195	0.3577	0.1908
0.07	18F*	46.4878	41.7578	9.1227	0.8983	0.0142	0.0019	0.0611	0.1323	-0.5827
0.1	18B*	45.8380	41.1894	9.0603	0.8986	0.0213	0.0043	0.0924	0.2014	-1.1364
0.1	192	3.9856	0.4868	0.9849	0.1221	0.0284	0.0204	0.2016	0.7187	0.0208
0.2	18E*	50.3230	50.0241	9.9846	0.9940	0.2184	0.1890	0.6137	0.8650	-0.2863
0.2	18F	15.7560	1.1100	1.4874	0.0705	0.3030	0.2824	0.7502	0.9322	-0.0523
0.3	18B	6.5057	2.4902	2.2278	0.3828	1.5229	1.4318	1.6893	0.9402	-0.0515
0.3	192*	48.8476	46.4824	9.6249	0.9516	1.3570	1.3175	1.6204	0.9709	-0.0962
0.4	18E*	53.2140	48.7383	9.8557	0.9159	4.3049	4.1871	2.8887	0.9726	-0.0931
0.4	18F	13.1134	6.3053	3.5449	0.4808	4.5796	4.5010	2.9951	0.9828	-0.0543

		Inertial Horizontal				Linear Horizontal				
Freq (Hz)	TSS-DL	σ^2_{tot}	σ^2_{sig}	a_{sig}	SNR	σ^2_{tot}	σ^2_{sig}	a_{sig}	SNR	a_{sig} % diff from analytic
0.07	18E	10.9520	2.9923	2.4421	0.2732	0.1080	0.0650	0.3599	0.6018	0.7313
0.07	18F*	44.3803	42.0200	9.1512	0.9468	0.1432	0.0955	0.4363	0.6672	0.7784
0.1	18B*	46.5363	44.4959	9.4170	0.9562	0.2378	0.1849	0.6070	0.7775	0.6748
0.1	192	9.4124	2.0143	2.0036	0.2140	0.1153	0.0734	0.3826	0.6371	0.4841
0.2	18E*	47.7025	47.4408	9.7236	0.9945	0.1717	0.1180	0.4849	0.6870	-0.6280
0.2	18F	16.1004	2.5755	2.2656	0.1600	0.2509	0.2027	0.6356	0.8079	-0.2420
0.3	18B	10.8863	1.9556	1.9742	0.1796	1.2849	1.1745	1.5299	0.9141	-0.1611
0.3	192*	47.0826	44.9845	9.4686	0.9554	1.3518	1.2616	1.5857	0.9333	-0.1202
0.4	18E*	47.3614	43.7046	9.3329	0.9228	3.7749	3.6299	2.6897	0.9616	-0.1740
0.4	18F	18.3975	5.4895	3.3076	0.2984	4.8070	4.6916	3.0578	0.9760	-0.0327

* indicated TSS-DL fully inverted during each revolution

THIS PAGE INTENTIONALLY LEFT BLANK

VI. FIELD APPLICATION

In late May through early June 2013, personnel from NPS on board research vessel (R/V) Point Sur conducted field experiments in the vicinity of the mouth of the Columbia River (MCR) (see Figure 31) in order to collect robust, in-situ surface wave data to further the study and understanding of wave-current interaction. During these experiments, WRD-Bs equipped with TSS-DLs were deployed from R/V Point Sur in the main channel of the MCR just prior to max ebb current to collect surface wave data as they drifted through the highly volatile entrance to the MCR, where large, often breaking waves are generated as the fast flowing ebb current encounters the incoming ocean swell over the relatively shallow bar. Figure 32 shows the significant wave height data recorded by a cluster of WRD-Bs deployed on June 8, 2013. This figure clearly captures this event where waves with heights near four meters are recorded.

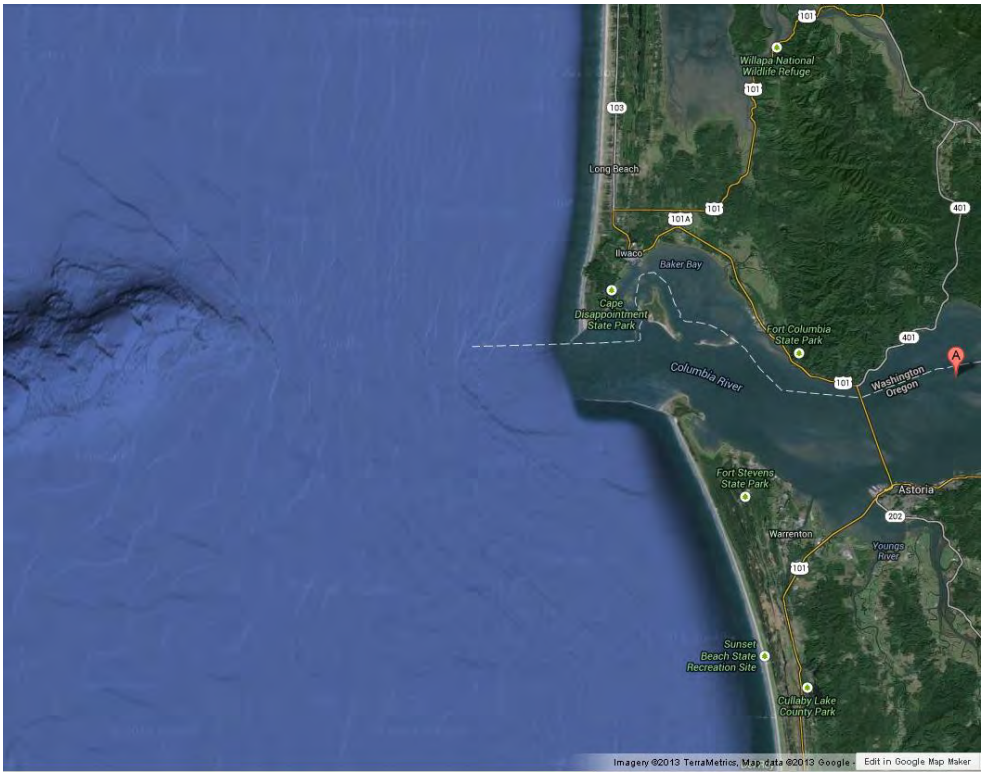

Figure 31. Mouth of the Columbia River (from Google 2013).

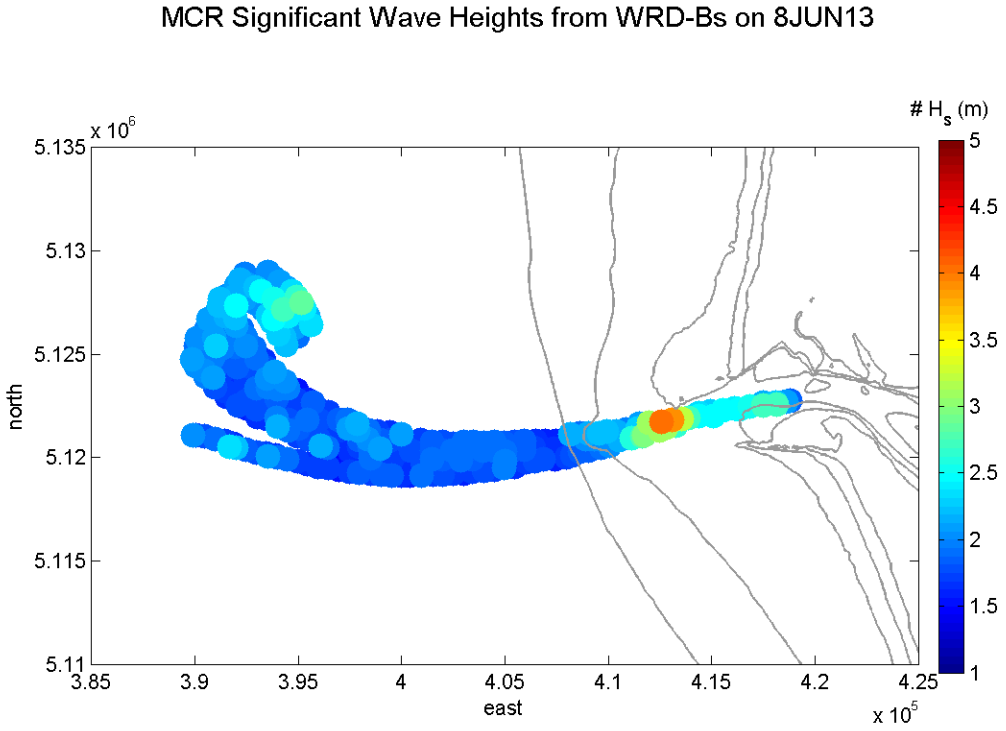

Figure 32. Significant wave heights from WRD-Bs in the MCR on June 8, 2013.

Figure 33 shows a section of surface wave height data just outside the MCR recorded by a WRD-B on June 12, 2013. This figure highlights the differences in surface wave heights from inertial (i.e., not transformed) and linear (i.e., transformed) data, which are seen here to differ by one meter or greater.

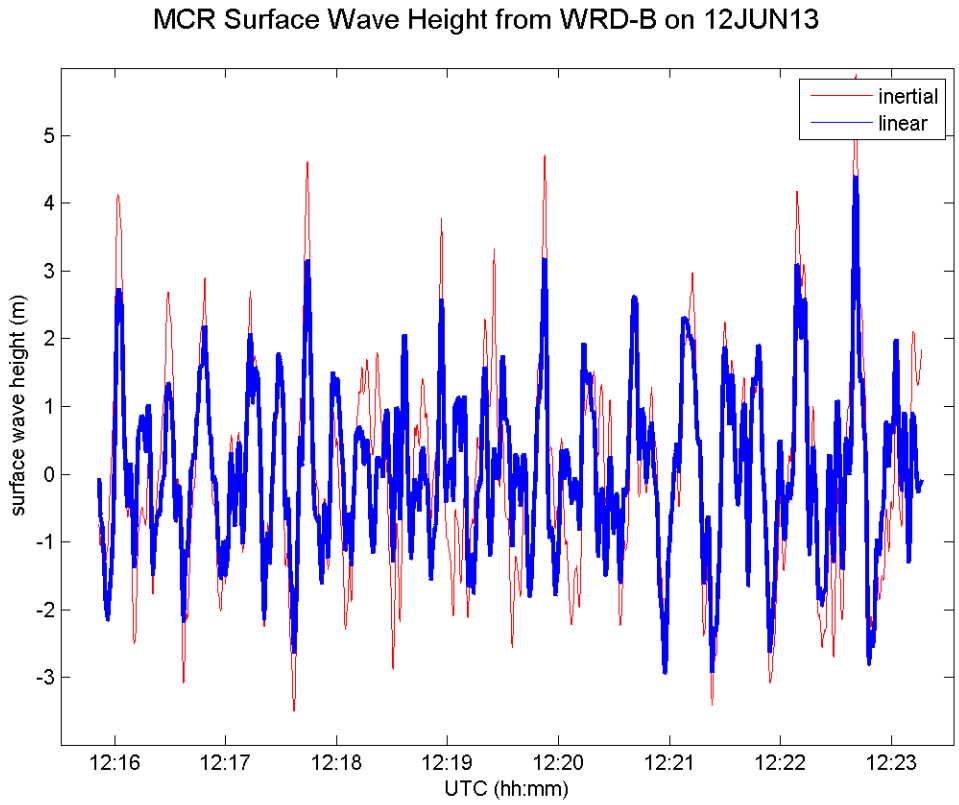

Figure 33. Inertial and linear surface wave height data from WRD-B outside the MCR on June 12, 2013.

Similar to Figure 33, Figure 34 shows the difference between the surface wave heights from inertial and linear data, this time in a case of large contamination from gravity present in the inertial surface wave heights due to extreme pitch/roll of the WRD-B. This figure illustrates the large errors that can be present in inertial (i.e., not transformed) data when the drifter encounters steep breaking or near-breaking waves, as well as the TSS-DL's ability to track the wave motion in these extreme conditions through its transformation algorithm.

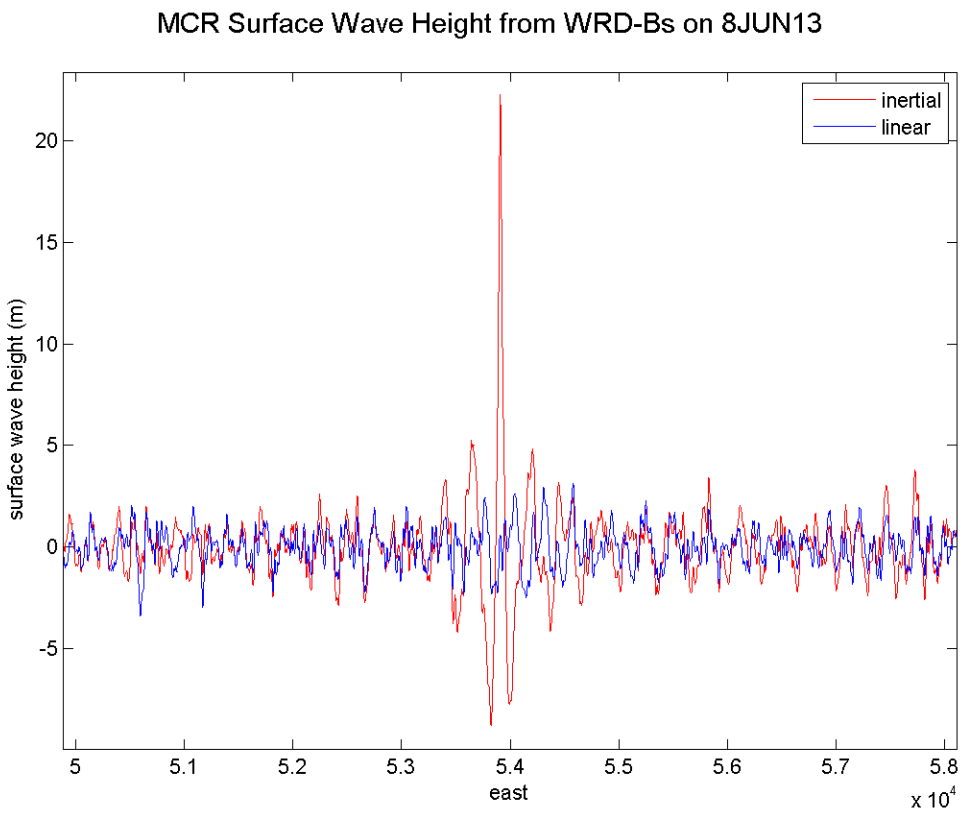

Figure 34. Extreme difference in surface wave height from inertial and linear data outside the MCR on June 8, 2013.

Lastly, Figure 35 shows the surface height spectra from a four hour record of a WRD-B that was deployed and recovered in deep water outside the MCR. Plotted are the spectral curves from the GPS receiver's Doppler velocity data, the WRD-B's inertial data, and the WRD-B's linear data. While the spectra agree fairly well at the dominant swell frequencies, the most significant difference is in the noise between the inertial and linear data below 0.1Hz. The inertial data contains significantly more noise as a result of amplification due to noise associated with tilt at low frequencies, thus making it more difficult to distinguish true wave signals from noise.

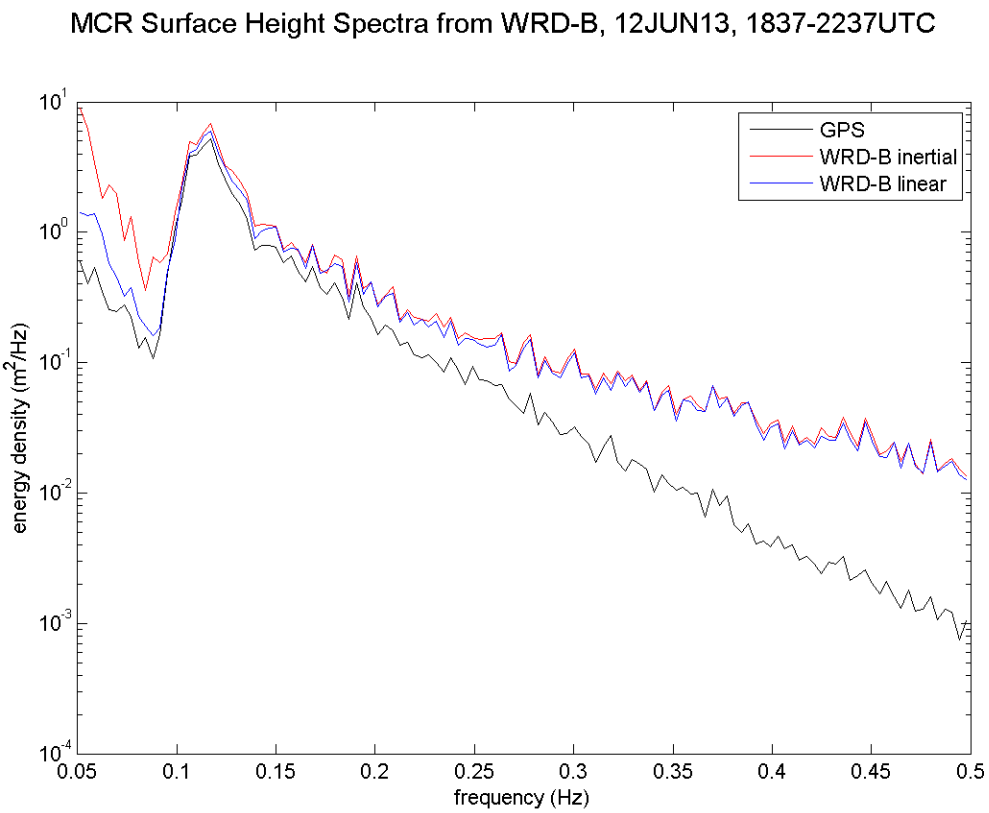

Figure 35. Surface height spectra from WRD-B in deep water outside the MCR on June 12, 2013.

THIS PAGE INTENTIONALLY LEFT BLANK

VII. CONCLUSIONS

The need for in-situ ocean surface wave data is great, particularly in coastal inlets and river mouths where both commercial shipping and the U.S. Navy operate. Collecting this data with traditional bottom mounted or moored instruments can be costly and logistically challenging owing to heavy ship traffic, energetic wave and current conditions, and dynamic seafloor morphology. While the use of GPS drifters equipped with COTS components has improved these collection efforts, the need for low-cost yet accurate wave sensors requires more research that is addressed in this thesis.

The Naval Postgraduate School (NPS) has been working toward developing low-cost and easily deployable wave resolving drifters (WRDs) for collecting surface wave data. The earliest prototype WRD-A proved to be a capable platform for deploying instruments to collect surface wave data; however, there remained room for improvement in its ability to accurately resolve surface wave motions, particularly in the vertical axis. The latest variant of this drifter, the WRD-B, incorporates Yost Engineering Incorporated's (YEI) 3-Space Sensor Data-Logging (TSS-DL) as the primary sensor for recording surface wave motion. The TSS-DL is a miniature attitude and heading reference system that is able to transform inertial data collected in its body reference frame into linear data referenced to the terrestrial reference frame through the use of quaternions and a specific algorithm, thereby making it useful for analysis.

To validate the TSS-DL's performance, we created a surface wave orbital motion simulator (SWOMS) on which to test the TSS-DL in a laboratory setting at NPS. Tests were conducted at five different frequencies within the dominant swell and wind-sea bands and were performed in different configurations varying the horizontal orientation and the degree of pitch/roll noise contamination. For each test we utilized the TSS-DL acceleration data to derive power spectral densities and displacements. From these we specifically analyzed the total and signal variances, the signal amplitude, and the signal to noise ratio of the total and signal variances. All parameters were then compared to the parameters generated from the known analytic motion of the SWOMS. Results from the test data showed that the TSS-DL is able to resolve the vertical signal amplitude to within

$\pm$ 3–7% of the analytic signal amplitude and is able to resolve the horizontal signal amplitude to within $\pm$ 21–33% of the analytic signal amplitude.

We further analyze field data collected by the TSS-DL onboard WRDs deployed in June 2013 near the mouth of the Columbia River. Results from this data show the TSS-DL is able to accurately resolve the vertical wave excursions it encountered even in extreme conditions with large breaking waves.

Overall, we have shown that the TSS-DL is a capable sensor appropriate for use in ocean surface drifters to accurately record surface waves. Future research related to this topic may include investigation into the customizable settings for the TSS-DL to see if there is room for improvement in noise reduction and increased accuracy of measurements. Additional testing may also be conducted at more frequencies and at varied amplitudes to further validate the performance of the TSS-DL in other conditions.

APPENDIX

Multiplication of two quaternions, $p = [p_0 \vec{p}]$ and $q = [q_0 \vec{q}]$ is defined as

$$p\ q = p_0 q_0 - \vec{p} \cdot \vec{q} + p_0 \vec{q} + q_0 \vec{p} + \vec{p} \times \vec{q} \tag{11}$$

The product of this multiplication is another quaternion of form $r = [r_0 \vec{r}]$ (from Calusdian 2010).

THIS PAGE INTENTIONALLY LEFT BLANK

LIST OF REFERENCES

Bachmann, E. R., 2000: Inertial and magnetic tracking of limb segment orientation for inserting humans into synthetic environments. Dissertation, Naval Postgraduate School, 195 pp.

Calusdian, J., 2010: A personal navigation system based on inertial and magnetic field measurements. Dissertation, Naval Postgraduate School, 235 pp.

Datawell BV, cited 2010: Datawell Waverider reference manual (WR-SG, DWR-MkIII, DWR-G). [Available online at http://www.datawell.nl/Portals/0/Documents/Manuals/datawell_manual_dwr-mk3_dwr-g_wr-sg_2010-07-28.pdf.]

Datawell BV, cited 2013: Buoys. [Available online at http://www.datawell.nl/products/buoys.aspx.]

Davis, R. E., 1991: Lagrangian ocean studies. *Annu. Rev. Fluid Mech.*, **23**, 43–64.

Free Wallpapers, cited 2013: Ferris wheel pictures. [Available online at http://fin6.com/2013/09/ferris-wheel-pictures/.]

Google, cited 2013: Google maps. [Available online at https://maps.google.com/.]

Herbers, T. H. C., P. F. Jessen, T. T. Janssen, D. B. Colbert, J. H. MacMahan, 2012: Observing ocean surface waves with GPS-tracked buoys. *J. Atm. Ocean. Tech.*, **29**, 944–959.

Janssen, T. T. & T. H. C. Herbers, 2009: Nonlinear wave statistics in a focal zone. *J. Phys. Oceanogr.*, **39**, 1948–1964.

Johnson, D., R. Stocker, R. Head, J. Imberger, and C. Pattiaratchi, 2003: A compact, low-cost GPS drifter for use in the oceanic nearshore zone, lakes, and estuaries. *J. Atm. Ocean. Tech.*, **20**, 1880–1884.

MacMahan, J., J. Brown, and E. Thornton, 2009: Low-cost hand-held global positioning system for measuring surf-zone currents. *J. Coastal Res.*, **25** (3), 744–754.

McIntyre, S. A., 2013: Wave and current observations in a tidal inlet using GPS drifter buoys. Thesis, Dept. of Oceanography, Naval Postgraduate School, 99 pp.

Pearman, D. W., T. H. C. Herbers, T. T. Janssen, S. F. McIntyre, and P. F. Jessen, 2013: GPS and accelerometer equipped drifters for observing ocean surface waves and currents. *Cont. Shelf Res.*, in press.

Schmidt, W. E., B. T. Woodward, K. S. Millikan, R. T. Guza, B. Raubenheimer, and S. Elgar, 2003: A GPS-tracked surf zone drifter. *J. Atm. Ocean. Tech.*, **20**, 1069–1075.

Solutions Cubed, cited 2013a: Motion Mind 3 ASCII control software. [Available online at http://www.solutions-cubed.com/content/Downloads/MotionMind3Docs/AN1007.pdf.]

Solutions Cubed, cited 2013b: Motion Mind 3 motor controller data sheet (Rev. 6). [Available online at http://www.solutions-cubed.com/content/Downloads/MotionMind3Docs/MOTM3DS_6.pdf.]

Thurman, H. V., 1988: *Introductory Oceanography 5th Edition*. Merrill, 515 pp.

YEI Technologies, cited 2013a: *3-Space Sensor Data-Logging user's manual*. [Available online at http://www.yeitechnology.com/sites/default/files/YEI_3-Space_Sensor_Users_Manual_DataLogging_2.0_r13_28Aug2013.pdf.]

YEI Technologies, cited 2013b: *3-Space Sensor suite manual*. [Available online at http://www.yeitechnology.com/sites/default/files/YEI_3-Space_Sensor_Suite_Manual_2.0_r11_26Jun2013.pdf.]

INITIAL DISTRIBUTION LIST

1. Defense Technical Information Center
   Ft. Belvoir, Virginia

2. Dudley Knox Library
   Naval Postgraduate School
   Monterey, California